



An investigation of the field-aligned currents associated with a large-scale ULF wave in the morning sector

H.C. Scoffield^{a,*}, T.K. Yeoman^a, D.M. Wright^a, S.E. Milan^a, A.N. Wright^b, R.J. Strangeway^c

^aDepartment of Physics and Astronomy, University of Leicester, University Road, Leicester, LE1 7RH, UK

^bUniversity of St. Andrews, St. Andrews, UK

^cUniversity of California, Los Angeles, CA, USA

Received 25 August 2005; accepted 4 April 2006

Available online 21 December 2006

Abstract

Previous work by Scoffield, H.C., Yeoman, T.K., Wright, D.M., Milan, S.E., Wright, A.N., Strangeway, R.J. [2005. An investigation of the field aligned currents associated with a large scale ULF wave using data from CUTLASS and FAST. *Ann. Geophys.* 23, 487–498] investigated a large-scale ULF wave, occurring in the dusk sector (~ 1900 MLT). The wave had a period of ~ 800 s (corresponding to 1.2 mHz frequency), an azimuthal wave number of ~ 7 and a full-width at half-maximum (FWHM) across the resonance of 350 km. IMAGE ground magnetometer and SuperDARN radar observations of the wave's spatial and temporal characteristics were used to parameterise a simple, two-dimensional field line resonance (FLR) model. The model-calculated field-aligned current (FAC) was compared with FACs derived from the FAST energetic particle spectra and magnetic field measurement. Here the authors use the same method to investigate the FAC structure of a second large-scale ULF wave, with a period of ~ 450 s, occurring the dawn sector (~ 0500 MLT) with an opposite sense background region 1-region 2 current system. This wave has a much larger longitudinal scale ($m \sim 4.5$) and a smaller latitude scale (FWHM = 150 km). Unlike the dusk sector wave, which was dominated by upward FAC, FAST observations of the dawn sector wave show an interval of large-scale downward FAC of $\sim 1.5 \mu\text{A m}^{-2}$. Downgoing magnetospheric electrons with energies of a few keV were observed, which are associated with upward FACs of $\sim 1 \mu\text{A m}^{-2}$. For both wave studies, downward currents appear to be carried partially by upgoing electrons below the FAST energy detection threshold (5 eV), but also consist of a mixture of hotter downgoing magnetospheric electrons and upgoing ionospheric electrons of energies 30 eV–1 keV. Strong intervals of upward current show that small-scale structuring of scale ~ 50 km has been imposed on the current carriers. In general, this study confirms the findings of Scoffield, H.C., Yeoman, T.K., Wright, D.M., Milan, S.E., Wright, A.N., Strangeway, R.J. [2005. An investigation of the FACs associated with a large-scale ULF wave using data from CUTLASS and FAST. *Ann. Geophys.* 23, 487–498]. © 2006 Elsevier Ltd. All rights reserved.

Keywords: Magnetosphere ionosphere coupling; Field line resonances; Particle acceleration; Field-aligned currents

1. Introduction

Ultra-low-frequency (ULF) magnetohydrodynamic (MHD) waves provide a mechanism for coupling between the magnetosphere and ionosphere allowing the transfer of energy and momentum, with these processes being strongest at high latitudes. They may be excited by processes external to the magnetosphere such as the Kelvin–Helmholtz instability at the flank magnetopause,

external solar wind impulses or internal mechanisms, for example particle-driven waves (through the drift and drift–bounce resonance processes). The resulting quasi-sinusoidal magnetic disturbances may be recorded by magnetometers, both on Earth and on orbiting spacecraft, whilst the associated electric fields may be measured by ground-based radar techniques.

The polarisation characteristics of ULF waves were initially observed using ground-based magnetometer arrays (Sugiura and Wilson, 1964; Samson and Rostoker, 1972) and led directly to the development of the theory of field line resonances (FLRs) (Southwood, 1974; Chen and

*Corresponding author. Tel.: +116 252 2083; fax: +116 252 3555.

E-mail address: hcs9@ion.le.ac.uk (H.C. Scoffield).

Hasegawa, 1974a, b). Subsequently, radars have been used to make more direct observations and provide improved spatial resolution (e.g. Walker et al., 1979). Recently detailed observations of both large- and small-scale ULF waves have been made using HF radar (Ruohoniemi et al., 1991; Walker et al., 1992; Fenrich et al., 1995; Fenrich and Samson, 1997; Wright and Yeoman, 1999; Yeoman and Wright, 2001; Baddeley et al., 2002), including observations of optical auroral modulation by ULF wave currents (Samson et al., 1991, 1992, 1996; Liu et al., 1995; Xu et al., 1993; Milan et al., 2001).

In situ spacecraft observations are also an important diagnostic of the ULF wave field. Satellite instrumentation provides a wealth of data allowing the improvement of theory through statistical studies (e.g. Anderson et al., 1990), with the majority of data suitable for the characterisation of ULF wave fields coming from spacecraft orbiting in high altitude, elliptical orbits. The FAST satellite is a low altitude spacecraft, capable of recording high temporal and hence spatial resolution measurements of the wave electric and magnetic fields and particle precipitations, which may be used to determine the large- and small-scale currents associated with a ULF wave. Recent work on such field-aligned current (FAC) measurements, which has concentrated mainly on steady-state FACs rather than those associated with wave fields, has been described in greater detail in Scofield et al. (2005). The gradient of the magnetic fields and the particle distributions may be used to infer the sense of the FAC or calculate the FAC density. (e.g. Carlson et al., 1998b; Elphic et al., 1998; Lotko et al., 1998; Peria et al., 2000). The resulting FAC densities of Elphic et al. (1998) show that both methods are in good agreement, with, in that case, FAC density of magnitudes in the region of $2\text{--}4 \mu\text{A m}^{-2}$.

While studies of FACs associated with ULF waves have been made, the particle acceleration processes, which greatly affect auroral processes, are not fully understood and are at present of considerable interest. The classical, one-fluid, MHD model of FLRs (e.g. Southwood, 1974; Chen and Hasegawa, 1974a, b) does not include parallel electric fields, which are required for the acceleration of auroral particles. Several authors have considered two-fluid models of FLRs and have attempted to consider the effects of the inclusion of finite electron inertia (inertial dispersion/inertial effects) and/or finite plasma temperatures (kinetic dispersion/kinetic effects) in more realistic magnetic field geometries (e.g. Streltsov and Lotko, 1995, 1996, 1997, 1999b; Streltsov et al., 1998; Rankin and Tikhonchuk, 1998; Rankin et al., 1999a, b, 2000; Wright et al., 2002; Wright and Hood, 2003). Where inertial and kinetic effects become important within FLRs, they can contract down to scale sizes of a few kilometres or even sub-kilometer scales with parallel electric fields sufficient to provide the electron acceleration necessary to drive discrete auroral arcs (Streltsov et al., 1998; Rankin and Tikhonchuk, 1998). At $L = 7.5$, accelerating electric fields, resulting in potentials of kV were estimated by Streltsov et al. (1998) to extend

out to $4R_E$ in altitude. More recent work by Wright et al. (2002) and Wright and Hood (2003) predicted that two fluid effects will result in the creation of parallel electric fields at an altitude of $\sim 1R_E$ above the ionosphere, energising electrons to $\sim 1 \text{ keV}$ for typical wave parameters.

Lotko et al. (1998) analysed an interval of FAST data which coincided with a 1.3 mHz FLR identified in ground radar and magnetometer data. They compared the data with the results of their linear dispersive FLR model, using a model FLR period of 88 s (corresponding to 11.4 mHz frequency) and added an anomalous resistivity layer to their model which resulted in the formation of a highly localised electric field which was consistent with FAST observations. The model used was not constrained by the ground data, which unfortunately was not presented in Lotko et al. (1998), but was fitted to the FAST observations themselves. Lotko et al. (1998) presented some interesting results concerning the acceleration process which takes place within FLRs, showing that the resonance powers upgoing and downgoing superthermal electron fluxes, a 10-km-wide auroral arc and an embedded electrostatic shock.

Previous work conducted by Scofield et al. (2005) concentrated on combining ground-based measurements of the large-scale structure of a ULF wave in the dusk sector from the CUTLASS coherent scatter radars and the IMAGE magnetometers with measurements of the small-scale structure made by the FAST satellite. A model of the large-scale structure of the FACs associated with the wave was constructed, using the mathematical formulations of Wright and Allan (1996) and the characteristics of the wave derived from ground-based data. The model was then compared with the large- and small-scale FACs measured by FAST's magnetic field instrument and particle detectors, revealing the small-scale structuring and energies of the current carriers in a large-scale Alfvén wave. The wave had a large latitudinal scale length, with a full-width at half-maximum (FWHM) of 350 km. The phase of the wave was such that FAST did not pass through a region of high intensity upward FAC. When FAST traversed a region of the wave involving low upward FAC densities, the current appeared to be carried by unstructured downgoing electrons of energies less than 30 eV. A downward current region appeared to be carried partially by upgoing electrons below the FAST energy detection threshold of 5 eV, but also consisted of a mixture of hotter downgoing magnetospheric electrons and upgoing ionospheric electrons of energies $< 30 \text{ eV}$, with the hotter upgoing electrons presumably representing those upgoing electrons which have been accelerated by the wave field above the low energy detection threshold of FAST. A stronger interval of upward current showed small-scale structuring of scale $\sim 50 \text{ km}$ had been imposed on the current carriers, which were downgoing magnetospheric electrons of energy 0–500 eV. This study provided an interesting insight into the small-scale structuring within the FAC structure associated with a large-scale ULF wave. However, study

of further events is required to confirm that this behaviour is common to large-scale FLRs. An initial search of data from January 1998 to December 2004 revealed ~ 3600 SuperDARN–FAST conjunctions. Ground data (radar and magnetometer) for each conjunction was examined by eye for signatures of FLRs. A preliminary investigation of 12 events, where $Pc5$ wave activity observed, was carried out and three of these events were identified as having sufficient ground data to parameterise the simple ULF wave model. Only one of the three events had data of comparable quality to that presented in Scoffield et al. (2005). The current work will attempt to apply the same techniques used in Scoffield et al. (2005) to this event, which occurs in the dawn sector, using data from the Saskatoon and Kapuskasing radars of the SuperDARN network and magnetometer data from the CANOPUS and Greenland networks. In this case the wave has a much smaller latitudinal scale, opposite sense background region 1-region 2 FAC, and FAST observes a region of higher intensity upward FAC. Whilst it was thought that the dusk sector wave of Scoffield et al. (2005) was still in a transitional state, the wave under study here appears to be in a steady state. The results of the analysis will be compared with the analysis of the dusk sector wave.

2. Instrumentation

This study uses data from the CANOPUS and Greenland magnetometer networks, the Kapuskasing and Saskatoon coherent scatter radars of the SuperDARN network and the FAST satellite.

2.1. The magnetometer networks

The Canadian Auroral Network for the OPEN Programme Unified Study (CANOPUS) (Samson et al., 1992) magnetometer network consists of 14 magnetometer stations; Located throughout Canada, covering a geographical latitudinal range of $53.86\text{--}69.54^\circ$ and a geographic longitude range of $220.89\text{--}267.89^\circ$. The greenland coastal magnetometer chain (Wilhjelm and Friis-Christensen, 1976) comprises of 17 magnetometer sites (12 in the west coast chain and five in the east coast chain) covering geographic latitudes and longitudes of $81.60\text{--}61.16^\circ$ and $290.77\text{--}343.33^\circ$, respectively. Each station uses fluxgate magnetometers (FGMs) to take measurements in three orthogonal directions with a sampling interval of 10 s, and a resolution of 1 nT.

2.2. The superDARN radars

The SuperDARN radar network currently comprises nine northern hemisphere radars and six southern hemisphere coherent HF radars (Greenwald et al., 1995). This study makes use of the Saskatoon, (52.16 geographic latitude (GLAT), 106.53 geographic longitude (GLON))

and Kapuskasing (49.39° GLAT and 82.32° GLON) radars, both located in Canada.

The SuperDARN radars measure the coherent backscatter of radio waves from ionospheric irregularities. The antennas in each array are phased to form an antenna pattern in which the maximum gain (beam position) has one of 16 azimuthal pointing directions separated by approximately 3.2° , distributed symmetrically about the radar boresites. In the normal scan mode of the radars, the 16 beams are sounded with a dwell time of either 3 or 7 s, producing field-of-view maps of backscatter, with an azimuthal coverage of over 50° , every 1 or 2 min. Typically, 75 range gates are sampled for each beam, with a pulse length of $300\ \mu\text{s}$, corresponding to a gate length of 45 km, and a lag to the first gate of $1200\ \mu\text{s}$ (180 km). In this configuration, the maximum range of the radars is approximately 3550 km, with each field-of-view containing 1200 cells (Greenwald et al., 1995). For the interval considered here, the standard mode of operation was used with a dwell time of 3 s. The auto-correlation function (ACF) of the backscatter radar signal is employed in order to produce a backscatter Doppler spectrum. The backscatter power, line-of-sight (l-o-s) velocity of scattering irregularities and spectral width imposed on the spectra may be derived from the ACF.

2.3. FAST

The NASA Fast Auroral SnapshoT (FAST) satellite (Carlson et al., 1998a) carries a range of scientific instruments that provide high spatial and temporal resolution measurements of charged particles and electric and magnetic fields within the low altitude auroral arc region. The satellite is spin stabilised, with a spin period of approximately 5 s, varying according to the conditions (e.g. time and temperature). It has an 83° inclination elliptical orbit ($350\ \text{km} \times 4175\ \text{km}$), crossing the auroral zones four times per orbit at different altitudes and positions. On-board instrumentation include electrostatic analysers (ESAs), electric field sensors, and magnetic field sensors.

The ESAs (Carlson et al., 2001) are used to measure the ion and electron pitch angle distributions for ions with energies between 3 eV and 25 keV, and electrons with energies between 4 eV and 30 keV. The 16 “top hat” analyser heads are grouped in pairs symmetrically spaced around the satellite, providing a 360° field of view. Deflection plates are used to steer the field of view in the measured magnetic field direction.

The spacecraft carries two magnetic field sensors; a FGM, mounted on a boom 2 m from the space craft, measuring the field along three axes; and an AC search-coil magnetometer, measuring AC magnetic field data between 10 Hz and 2.5 kHz on two axes and up to 500 kHz on the third axis (Ergun et al., 2001).

3. Observations

On 3 December 2001, a large-scale ULF wave was observed in the dawn sector (\sim 0500 MLT) simultaneously in the Saskatoon and Kapuskasing radars of the SuperDARN network, between 10:00 and 12:30 UT. The l-o-s velocity data from the Kapuskasing and Saskatoon radars is presented in the right-hand columns of Figs. 1 and 2, respectively. The left-hand columns show model data which will be discussed in detail in Section 4. The magnitude of the velocities are colour coded, ranging from blue (1000 m s^{-1}) to red (-1000 m s^{-1}). The corresponding velocities are indicated on the colour bars, positive velocities indicating motion toward the radar. The wave was also observed by the CANOPUS magnetometer network which is located beneath the radar fields of view and the Greenland magnetometer network which is located sunward of the radar sites. The locations of the magnetometer sites are indicated by the triangles on the map in Fig. 3 and the radar fields of view are marked with black lines. The radar line of site (l-o-s) velocities varied between $\pm 800 \text{ m s}^{-1}$ with a period of $\sim 450 \text{ s}$ (2.2 mHz).

The wave appears in magnetometer data between 1000 and \sim 1700 UT with the greatest intensities between 1000 and 1300 UT. The wave covered magnetic latitudes (MLATs) $69\text{--}75^\circ$ in the radar fields of view and was observed in all the available magnetometer data spanning geographic latitudes $58\text{--}70.5^\circ$ in CANOPUS and $66\text{--}85^\circ$ in Greenland, with magnetometer stations covering magnetic local times \sim 0000 to 1200 MLT. Fig. 4 shows data from the CANOPUS magnetometer network with the north-south (B_x) components and east-west (B_y) components of magnetic field for a set of stations at $\sim -29^\circ$ magnetic longitude (MLON), plotted in descending latitude. The mean of the data was subtracted from the time series and then a 10% cosine bell function was applied to the start and end of each time series. The data were filtered using a time domain convolution with a Lanczos squared filter, using a high-frequency cutoff of 5 mHz (200 s) and low-frequency cutoff at 3.3 mHz (\sim 300 s). The wave signature is clearly visible in all stations. Fig. 5 shows data from the Greenland magnetometer network, again the B_x and B_y components are plotted for stations at $\sim 39^\circ$ MLON in order of descending MLAT and the wave signature is clearly visible. The locations of the magnetometer stations used in Figs. 4 and 5 are indicated on the map in Fig. 3 by the solid triangles. Using Fourier analysis, the wave frequency is determined to be $\sim 2.2 \text{ mHz}$; however, other less dominant frequencies exist (e.g. 1.1 mHz). This is discussed in greater detail in section 4. The wave amplitude appears to increase with latitude in CANOPUS data, with the largest amplitude observed in the highest latitude station, with available data, RAN, which is located at 73.2° MLAT. This indicates that the resonance is occurring at or above this latitude. The peak amplitude in Greenland data is easier to identify, lying at $\sim 74^\circ$ MLAT. However, since the Greenland chain is located $\sim 5\text{h}$ MLT sunward of the radars, the latitude of the resonance may not be consistent between the

two arrays. Analysis of the SuperDARN data confirms the wave frequency and indicates that the peak wave amplitude in the radar field of view is located between 71° and 73° MLAT.

The FAST satellite passed through the overlapping radar fields of view between \sim 1124 and 1140 UT, flying approximately North to South at an altitude of \sim 3600 km. The footprint of the satellite is indicated by the black line in Fig. 3. The locations of the Saskatoon and Kapuskasing radar fields of view are indicated by the letters t and k respectively. Data from the FAST instruments for 1120–1140 UT is presented in Fig. 6. The panels (a) and (b) show magnetic field measurements resolved in the northward (X) and eastward (Y) directions, respectively, plotted in black. The magnetic field values smoothed with a 20 s running mean window (corresponding to a FAST displacement of $\sim 50 \text{ km}$) are plotted in orange. The red traces indicate modelled values. The details of the model are presented in Section 4. Some of the large-scale magnetic field changes associated with the wave model, which is based on observations from ground instruments (magnetometers and radars) are observed in the data but there are also many small-scale features which are not present in the model. The magnetic field measurements show no obvious region 1–region 2 current pattern. The b_x component is initially $\sim 80 \text{ nT}$ and is directed northward but decreases rapidly, varying between $+20$ and -20 nT around the location of the resonance ($84\text{--}65^\circ$ MLAT). The b_y component is directed eastward (with positive values of $50\text{--}100 \text{ nT}$) throughout the interval. Panels (c)–(f) display the energetic particle spectra for electrons moving downwards, towards Earth (EESA down), electrons moving upwards (EESA up), ions moving downward (IESA down) and ions moving upward (IESA up) respectively. Panel (c) shows highly structured downward precipitating electrons, with energies of up to $\sim 1 \text{ keV}$. After $\sim 11:28:30$, when the spacecraft is at $\sim 80^\circ$ MLAT, moving into the auroral zone the structuring appears less pronounced and higher energy particles are observed. At $\sim 11:32:00$ ($\sim 75^\circ$ MLAT) particles have energies up to $\sim 10 \text{ keV}$. At $\sim 11:35:00$ ($\sim 71^\circ$ MLAT) the spacecraft experience a mode change. Beyond this point, the temporal resolution is much lower and as a result the fine structure is no longer visible within the data. The upward moving electron spectra, shown in panel (d), follow a similar pattern, with electron having slightly lower energies throughout. Patches of downwards precipitating ions with energies ranging from 100 eV to 10 keV are observed throughout the first part of the interval in panel e, becoming more numerous as FAST enters the auroral zone at $\sim 11:28:30$ ($\sim 80^\circ$ MLAT). Very few upward moving ions (displayed in panel f) are observed during the interval. The particle-derived current is plotted in black in panel g. The model-derived current is plotted in blue. The particle-derived current displays many small-scale features which correspond to those displayed in the particle and field data and will be discussed further in Section 5.

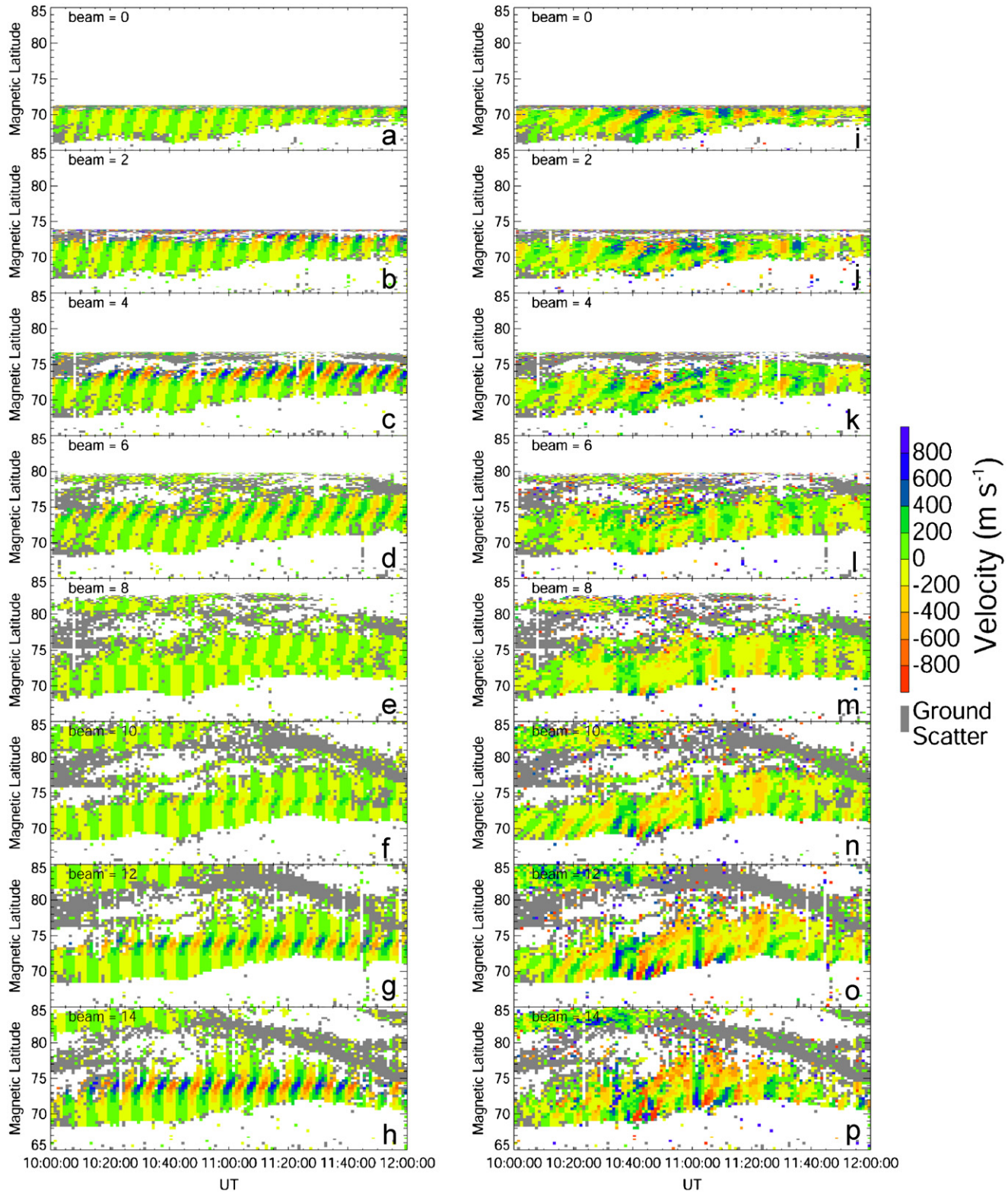


Fig. 1. (a)–(p) The right-hand panels represent Kapuskasing radar line-of-sight velocity data, beams 0, 2, 4, 6, 8, 10, 12 and 14, respectively, with the left-hand panels being the equivalent model plots (see text for details).

4. Model

Because of the short time taken for FAST to pass through the auroral zones, which is of the order of one

wave period of the event under analysis, and the temporal and spatial variations of the ULF wave field, it is not a trivial matter to correlate features in the FAST data with those in the SuperDARN data, where each beam has a

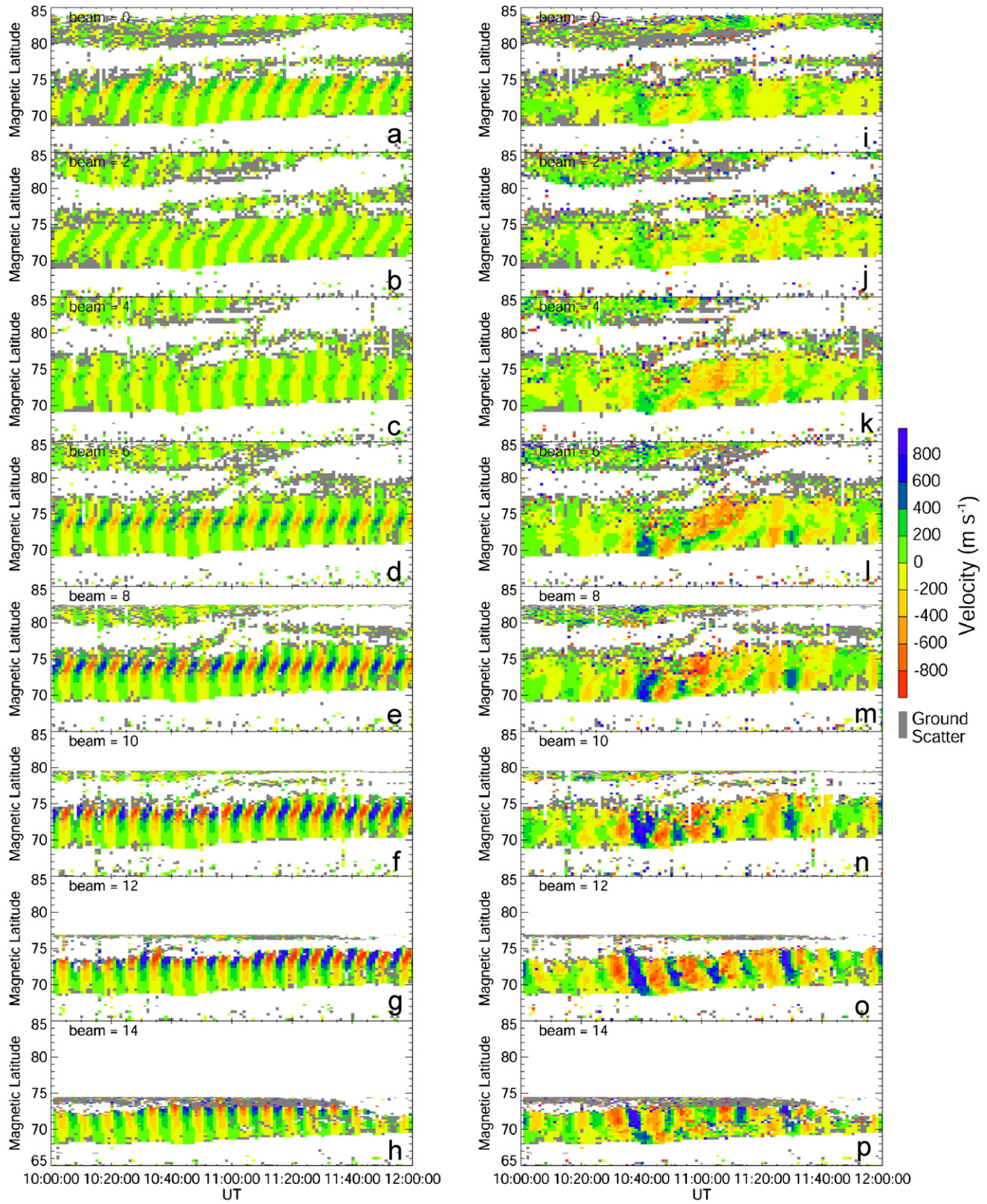


Fig. 2. (a)–(p) The right-hand panels represent Saskatoon Radar line-of-sight velocity data, beams 0, 2, 4, 6, 8, 10, 12 and 14, respectively, with the left-hand panels being the equivalent model plots (see text for details).

different look direction and therefore observes a different component of the velocity vector. In order to resolve these problems, a simple two-dimensional model (Wright and

Allan, 1996) was used to recreate various FAST parameters as a function of both time and position using the information from the ground-based observations. The

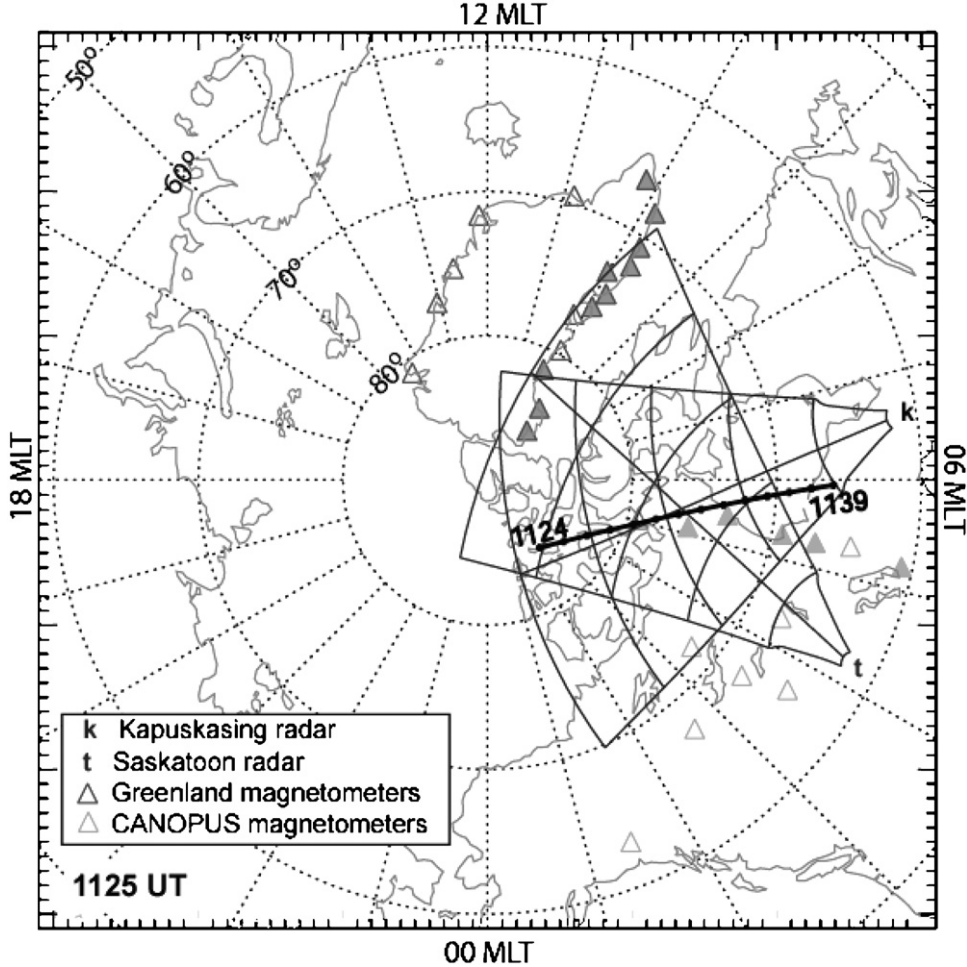


Fig. 3. Polar map plotted in magnetic coordinates for 1125 UT, showing the positions of the Saskatoon and Kapuskasing radar fields of view, labelled with 't' and 'k' respectively. The locations of the CANOPUS magnetometer stations are marked as grey triangles, the filled triangles indicate those stations which were used to produce Fig. 4. The black triangles indicate the locations of the Greenland magnetometer stations. The solid triangles indicate which stations were used to produce Fig. 5. The FAST satellites footprint is marked by the thick black line, the crosses represent 1 min intervals. The coastlines are marked in grey, with 0 MLT (midnight) located at the bottom of the plot, 12 MLT (noon) at the top, 6 MLT (dawn) to the right and 18 MLT (dusk) to the left.

basic model is described in Section 4.1 and the scaling and fitting of the model to the ground observations is described in Section 4.3.

4.1. The model

Wright and Allan (1996) presented an analysis of the structure, phase motion and heating which occurs within Alfvén resonances. They considered energy dissipation via two mechanisms, describing two different models. The first involved the addition of resistivity (η) within the body of the plasma and the second, the inclusion of finite Pedersen conductivity (Σ_P). The method of dissipation was found not to affect the structure and phase motion of the resonant fields. The spatially integrated dissipation rate was found to be independent of time for both mechanisms. The resistive boundary model (finite Σ_P) is used here to model the observed large-scale wave.

The model is based on the box model (e.g. Southwood, 1974) with perturbations varying as $\exp i(k_y y - \omega t)$, where \mathbf{k} is the wave vector, t is time, x is analogous to the meridional direction, y to the azimuthal direction and z to the radial direction. The standing waves on the field lines vary with z . The perturbation magnetic and electric fields are given by

$$b_x = -k_z \xi_x B, \quad (1)$$

$$b_y = -k_z \xi_y B, \quad (2)$$

$$E_x = i\omega \xi_y B, \quad (3)$$

$$E_y = i\omega \xi_x B. \quad (4)$$

The values of ξ_x and ξ_y are given by Eqs. (5) and (6) with Eqs. (7) and (8) defining the functions F and G and the variable X given by Eq. (9).

$$\xi_x = \xi_{x0} e^{i\phi} G(X), \quad (5)$$

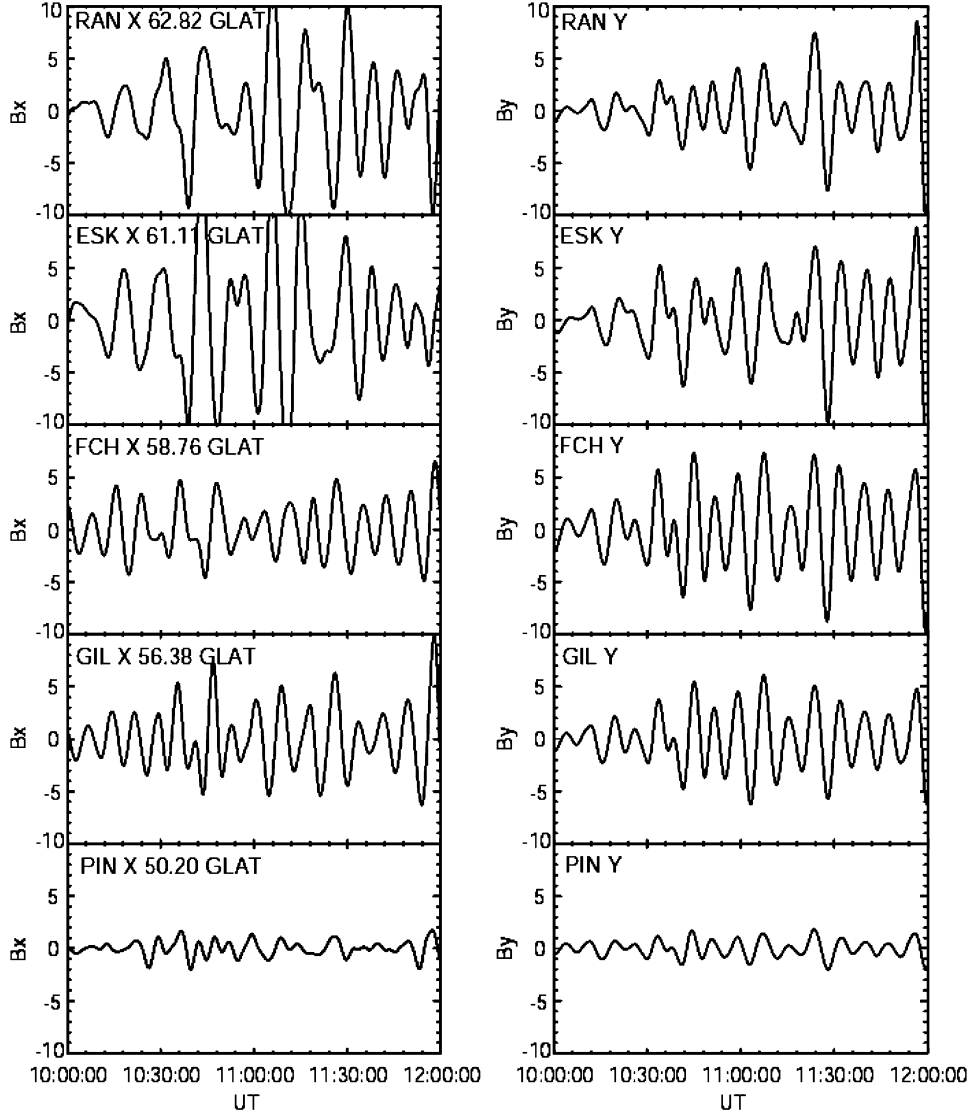


Fig. 4. Magnetic field data from CANOPUS stations, RAN, ESK, FCH, GIL and PIN. The left-hand panels present the north–south component (B_x) and the right-hand panels the east–west component (B_y) of magnetic field. The data was filtered with a high pass filter of 5.0 mHz and a low pass filter of 1.25 mHz. The locations of the stations are indicated by the solid triangles in Fig. 3.

$$\xi_y = -\xi_{x0} \frac{e^{i\phi}}{k_y \delta_b} F(X), \quad (6)$$

$$F(X) = -i/X - i, \quad (7)$$

$$G(X) = \ln(X - i), \quad (8)$$

$$X = x - x_r/\delta_b. \quad (9)$$

The variable x_r is the latitudinal location of the resonance, δ_b defines the latitudinal scale size of the model (the scale size in the x -direction), ξ_{x0} is given by Eq. 10 and b_{y0} defines the magnitude of the magnetic perturbation.

$$\xi_{x0} = b_{y0} k_y \delta_b / B k_z. \quad (10)$$

In the absence of any reliable measurements the height integrated Pederson conductivity was assumed to be 3S (a typical value at these latitudes, see Baddeley et al., 2002),

the background magnetic field \mathbf{B} , was assumed to be 5×10^4 nT and the initial amplitude of the perturbation magnetic field (b_{y0}) was set to be 150.0 nT from comparison of the model electric field amplitude and SuperDARN radar observations. The wave period, azimuthal wave number, location of the resonance (x_0), initial phase (y_0) and latitudinal scaling were all derived from analysis of the ground magnetometer and radar data, as outlined in Section 4.3.

4.2. Calculating the FACs

FAST observations and model output may be used to provide measurements of the FAC. Upward and downward particle fluxes are used to calculate the field-aligned flow of charge and hence the current. Values are typically of a few $\mu\text{A m}^{-2}$. Where FAC density values calculated

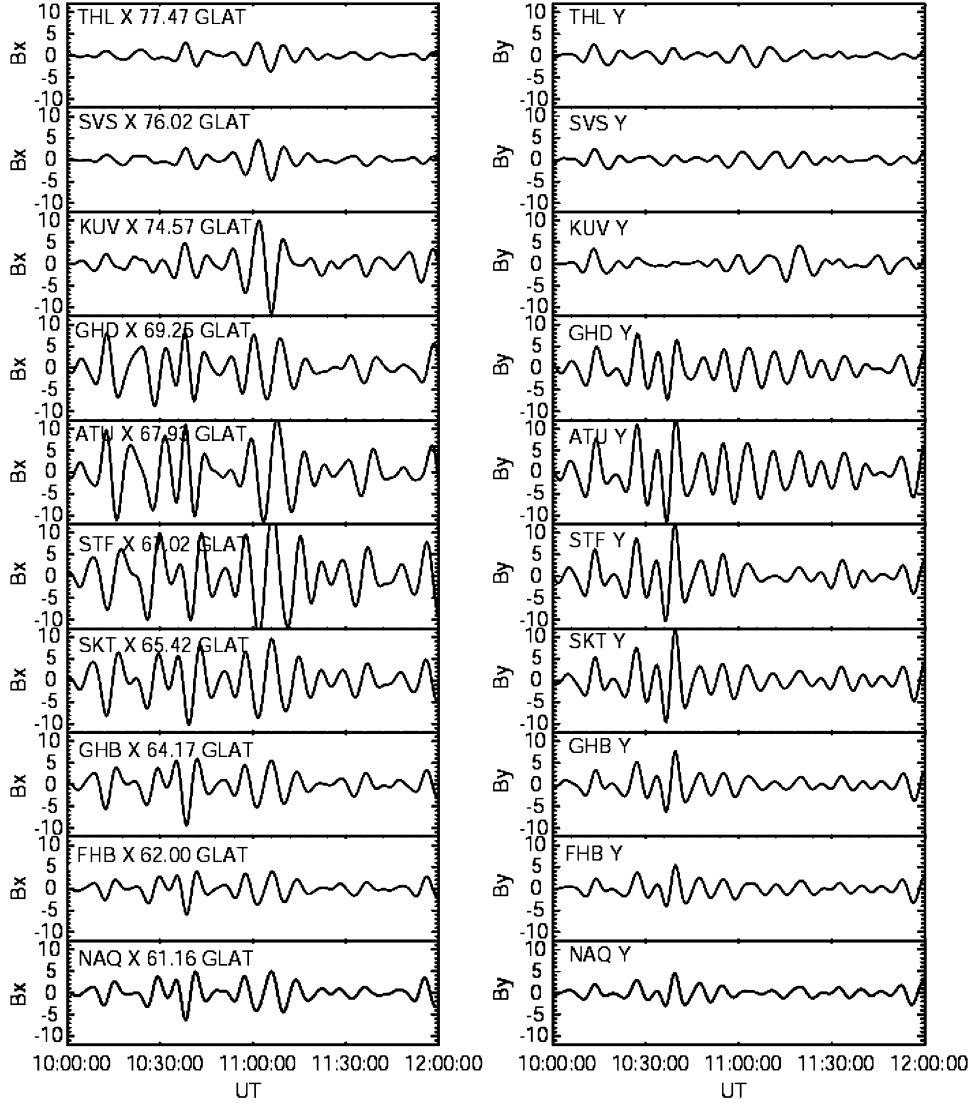


Fig. 5. Magnetic field data from Greenland network, stations, THL, SVS, KUV, GDH, ATU, STF, SKT, GHB, FHB, NAQ. The left-hand panels present the north-south component (B_x) and the right-hand panels the east-west component (B_y) of magnetic field. The data was filtered with a high pass filter of 5.0 mHz and a low pass filter of 1.25 mHz. The locations of the stations are indicated by the solid pink triangles in Fig. 3.

using particle fluxes are presented in this paper they will be referred to as the ‘particle-derived current’ or the ‘particle current’. The FAC density may also be calculated using the magnetic field measurements. There are two possible methods both making use of Eq. (11) below, where b_x and b_y are the X (north–south) and Y (east–west) components of the magnetic field perturbation \mathbf{b} and μ_0 is the permittivity of free space:

$$j_z = (1/\mu_0)(\nabla \times \mathbf{b})_z = \frac{1}{\mu_0} \left(\frac{\partial b_y}{\partial x} - \frac{\partial b_x}{\partial y} \right). \quad (11)$$

The first involves taking the component of magnetic field which is perpendicular to both the background magnetic field and the motion of the spacecraft, B_{perp} and the spacecraft’s displacement along its path, s . The FAC density j_z may be calculated using Eq. (11) in the form of

$$j_z = (1/\mu_0)(dB_{\text{perp}}/ds). \quad (12)$$

In order to do so it must be assumed that the spacecraft flies perpendicular to the current sheets. The second method involves using the northward (b_x) and eastward (b_y) components of the magnetic field directly in Eq. (11) along with the northward (dx) and eastward (dy) displacement of the satellite as it moves along its trajectory. This method requires the assumption that changes in b_x are only dependent on dy and changes in b_y are only dependent on dx , which is clearly not often the case. Both magnetic field methods yield very similar results with typical values of a few $\mu\text{A m}^{-2}$. The magnetic field-derived current and model-derived current values presented here have been calculated using Eq. (12).

4.3. Scaling and fitting the model

In order to scale the model to the observed wave parameters, longitude and latitude profiles of wave

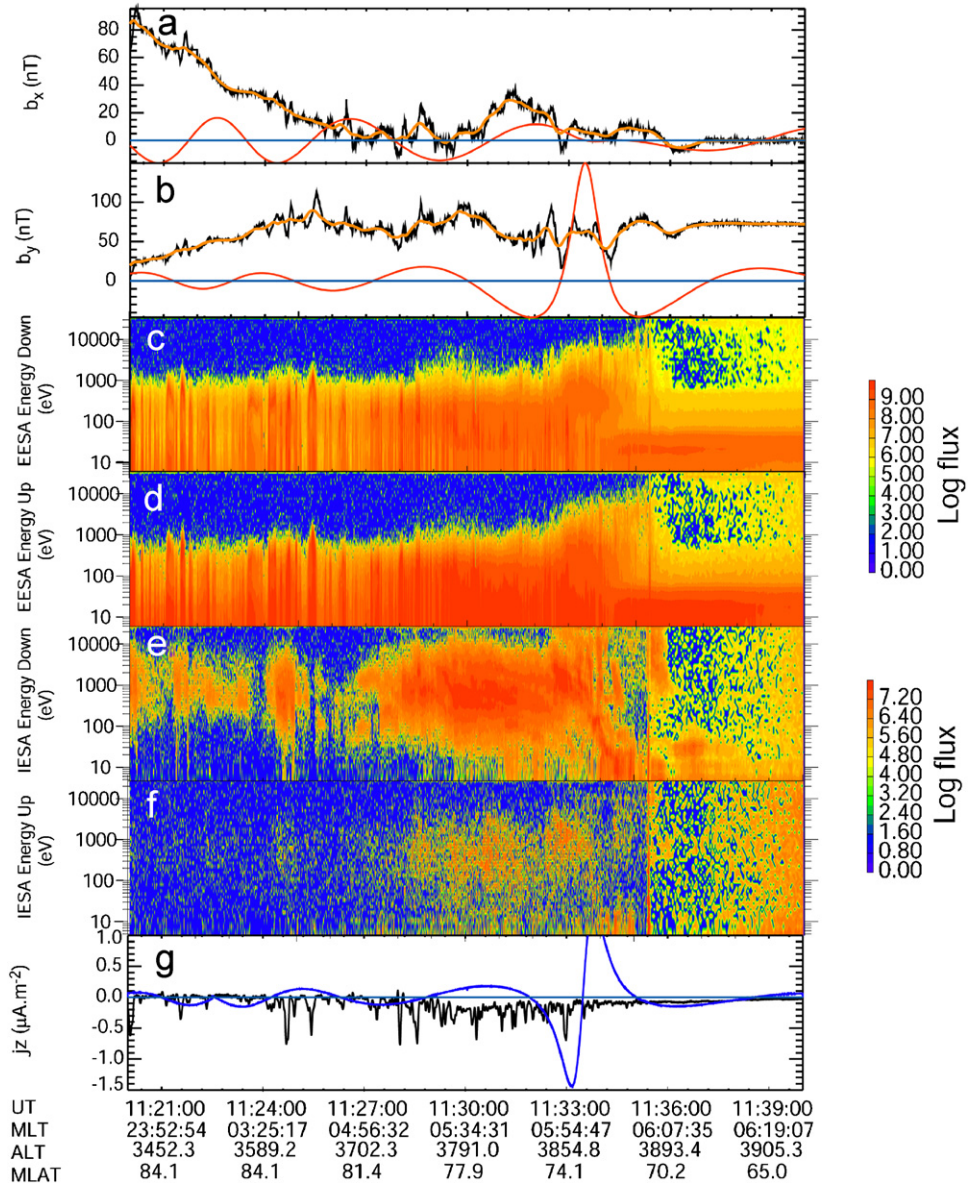


Fig. 6. (a) Magnetic field component in the north-south (x) direction. (b) Magnetic field component in the east-west (y) direction, the orange lines represent the measured data, smoothed with a 20 s running mean window, the red lines represent theoretical values and the blue lines represent the zero axis. (c) Energetic particle spectra for electrons moving downward relative to the spacecraft. (d) Energetic particle spectra for electrons moving upward e) Energetic particle spectra for ions moving downward. (f) Energetic particle spectra for ions moving upward. (g) The field-aligned current density calculated from the particle measurements. Here negative values represent upward field-aligned current.

amplitude and phase were required. To determine these profiles data from two sets of CANOPUS stations and two sets of Greenland stations, one set lying on a line of constant longitude and one lying on a line of constant latitude, were subjected to Fourier analysis. The profiles were created using data time series from 1100 to 1200 UT (presented in Figs. 4 and 5). The mean of the data was reduced to 0% and a 10% cosine bell function was applied to the start and end of each time series. The data were then processed, using a time domain convolution with a Lanczos squared filter, with a 1.25 mHz (800 s) high-frequency cutoff and a 3.3 mHz (\sim 300 s) low-frequency cutoff. Fourier analysis was used to identify the peak

spectral power, which occurs at 2.2 mHz (454 s) and the corresponding spectral phase. The Fourier power spectra for the CANOPUS and Greenland magnetometer data are shown in Figs. 7 and 8. The peak power and phase are plotted again latitude and longitude in Figs. 9–11 along with model traces for the magnetometer and radar data are discussed below.

The latitude profile for the Greenland magnetometer data (Fig. 9) displays the classic signature of a FLR, with a well-defined peak in power at 74° MLAT, indicating the location of the resonance and a change in phase of 180° across the resonance. This indicates that the wave observed is a FLR. The available CANOPUS data (presented in

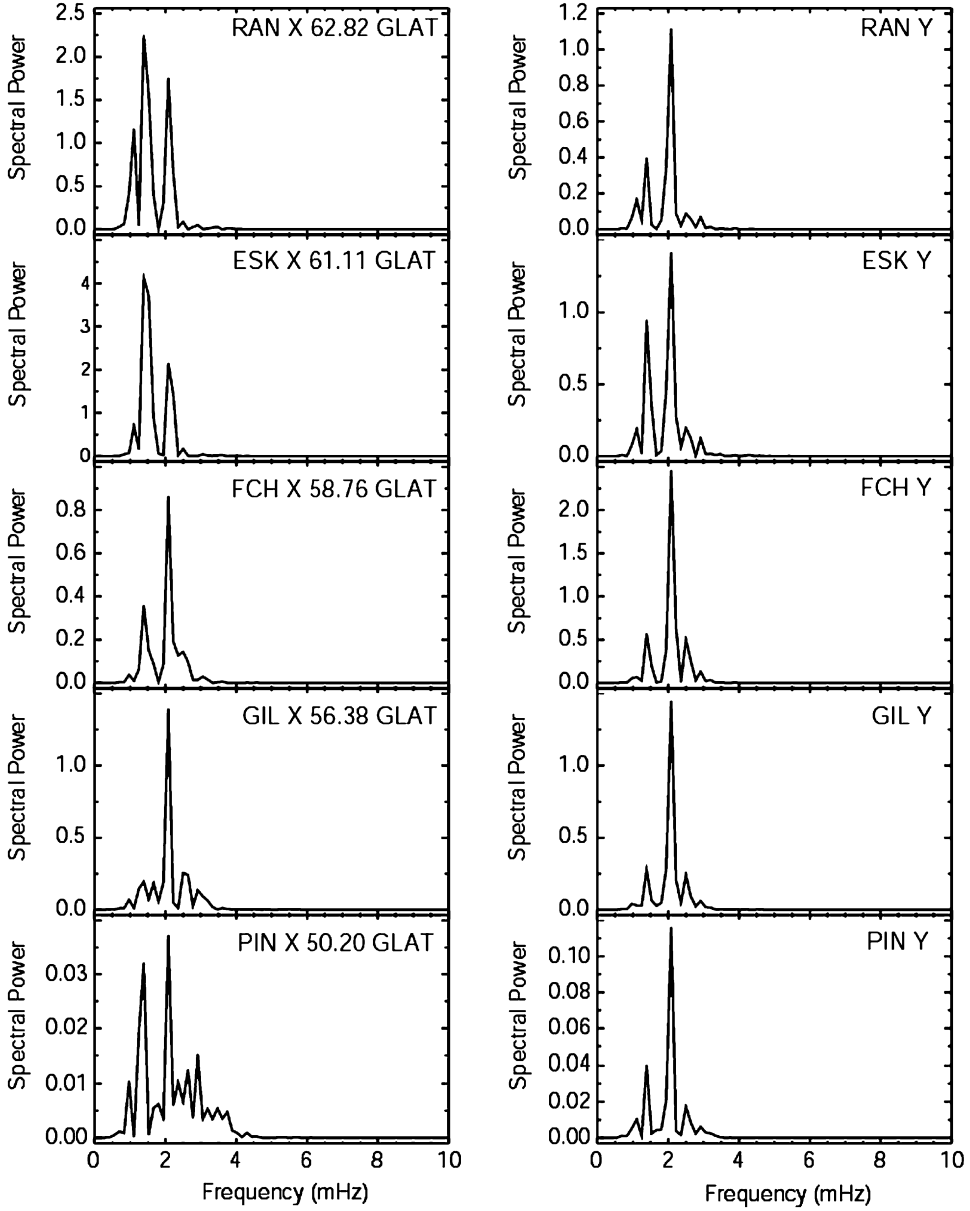


Fig. 7. The Fourier power spectra plots for the magnetic field data presented in Fig. 4, from CANOPUS stations, RAN, ESK, FCH, GIL and PIN. The locations of the stations are indicated by the solid green triangles in Fig. 3.

Fig. 4) covers a much smaller latitudinal range and hence the latitude profile (Fig. 10a) shows a less well-defined signature, with the peak in power occurring in the highest latitude data at the highest latitude station (73.2° MLAT), along with a corresponding change in phase. It is therefore only possible to conclude that the position of the resonance lies at 73° MLAT or above. Fig. 10b shows the longitude profiles for the CANOPUS magnetometer data, which displays a slow change in phase with longitude, indicating a small azimuthal wave number, $m \sim 3.5$. There are not enough Greenland magnetometer stations lying on a line of constant latitude to create a longitude profile. Comparison between Greenland and CANOPUS stations was attempted but aliasing issues proved difficult to resolve,

due to the large longitudinal separation between the two networks.

Two latitude profiles for the Kapuskasing radar, beam 11 and the Saskatoon radar, beam 5, which are both pointed approximately northwards, are presented in Figs. 11a and c, respectively. Using beam 11 from Kapuskasing and beam 5 from Saskatoon which are both pointed approximately northwards. As with the analysis of magnetometer data, data from 1100–1200 UT were filtered in the same way as the magnetometer data. The mean of the data was reduced to zero and a cosine bell function was applied to the start and end of each time series. A time domain convolution with a Lanczos squared filter was applied, using a 1.25 mHz (800 s) high pass filter and a

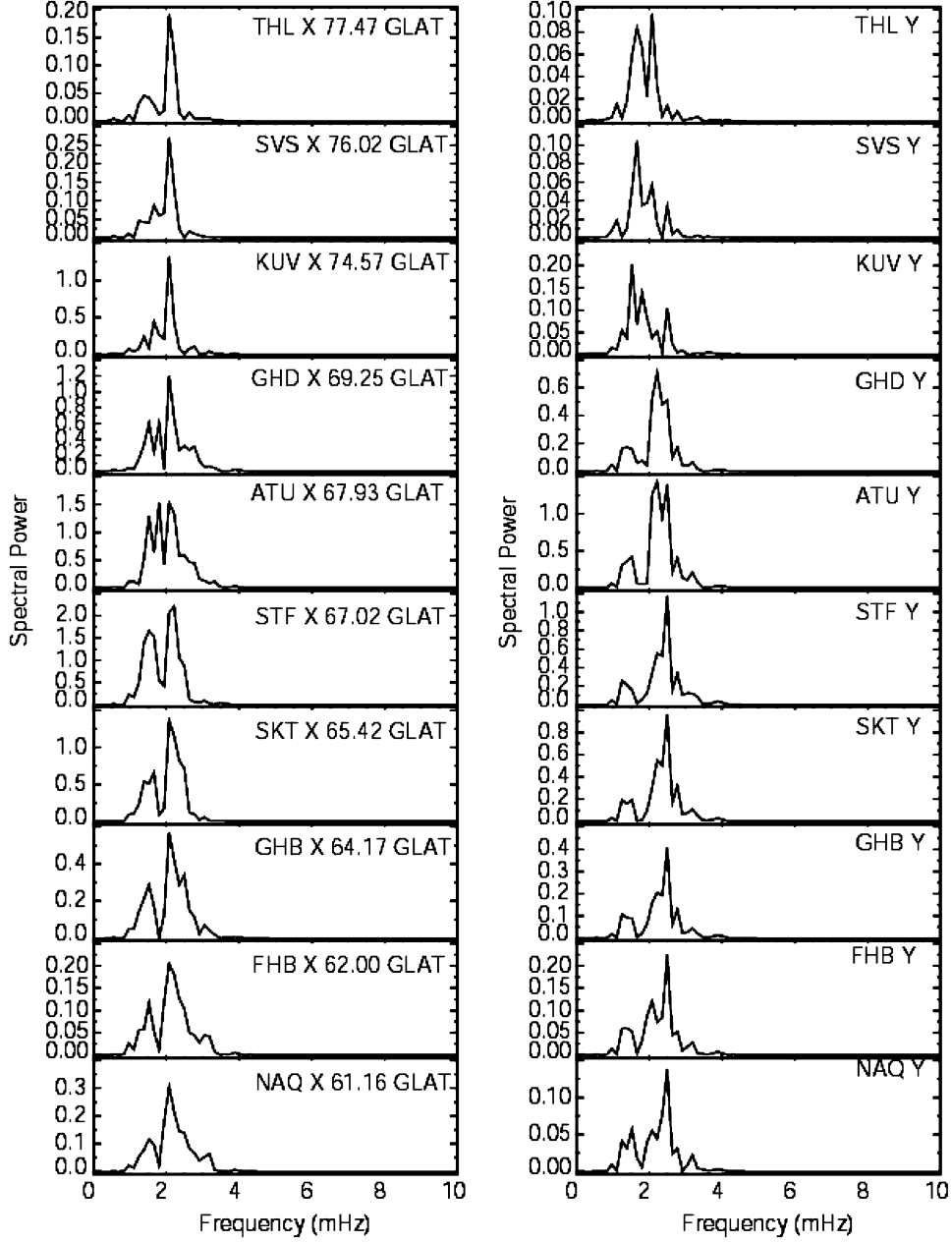


Fig. 8. Fourier power spectra plots for the magnetic field data presented in Fig. 5, from Greenland network, stations, THL, SVS, KUV, GDH, ATU, STF, SKT, GHB, FHB, NAQ. The locations of the stations are indicated by the solid pink triangles in Fig. 3.

3.3 mHz (~ 300 s) low pass filter. Fourier analysis was used to identify the peak spectral power, (at 2.2 mHz frequency, 454 s period) and the corresponding spectral phase. Both profiles show a peak in power and a corresponding change in phase of $\sim 180^\circ$. The profiles are not as smooth and well defined as the magnetometer profiles; however, the MLAT of the resonance appears to be at $\sim 73^\circ$ in Fig. 11a and $\sim 73.5^\circ$ in Fig. 11c which agrees with Fig. 9.

Panels b and d of Fig. 11 show examples of longitude profiles derived (as described above) from Kapuskasing and Saskatoon radar data, showing data from range gates 35 and 30 lying at approximately 73° and 70° MLAT, respectively. As expected the profiles show that the power

remains roughly constant across the field of view, while there is a slow change in phase with longitude. However, it is difficult to derive an m number from this plot because the phase is also sensitive to small changes in latitude between the same range gate on different radar beams. These profiles were, however, used to check the longitudinal scaling of the model which is discussed below.

The model was then scaled in latitude so that the size and shape of the profiles matched those of the observations, with a period 450 s, an azimuthal wave number, $m = 3.7$, corresponding to a longitudinal wavelength of ~ 3000 km, centred on 73.5° MLON providing the best fit. The model parameters are summarised in Table 1. The latitudinal

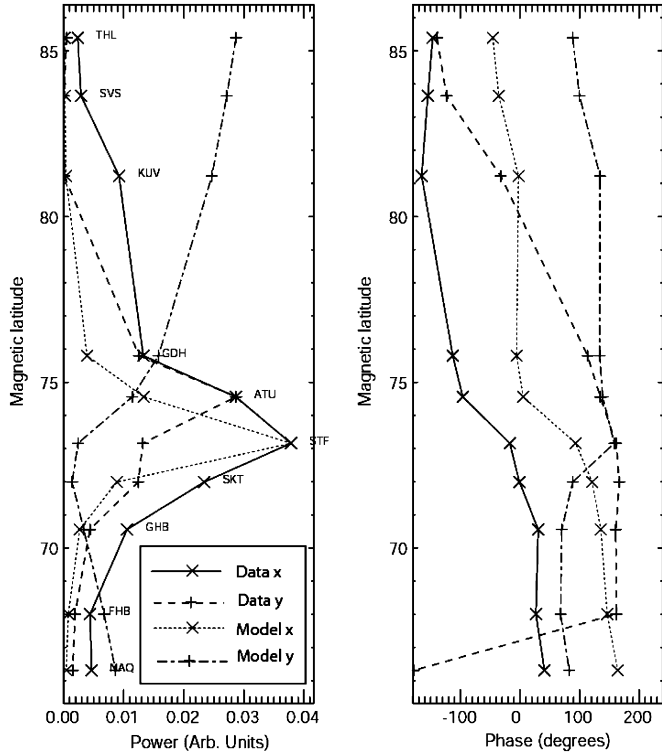


Fig. 9. Latitude profile power and phase plots for the Greenland magnetometer stations. The latitude profile is centred on $\sim -39^\circ$ MLON. The + signs represent the Y components and x signs representing the X components. The solid and dashed lines represent the data x and y components respectively. The dotted and dot-dashed lines represent the model x and y components respectively. For each of the profiles here the information was taken for the frequency 2.2 mHz from Fourier analysis of data for the time interval 11:00–12:30 UT.

scaling was chosen to best fit both the magnetometer and radar data curves resulting in a FWHM of ~ 160 km. The model was used to calculate the magnetic and electric field components, b_x , b_y , E_x , E_y and the FAC, j_z . The spatial variation of the Fourier analysis of the modelled wave parameters are over plotted on the latitude and longitude profiles of the magnetometer and radar data in Figs. 9–11. For the magnetometer data, the B_x component is plotted with a dotted line and the B_y component with a dot-dashed line. For the radar data, the diamonds represent the x component and the triangles the y component. The crosses represent the component resolved in the radar beam pointing direction, corresponding to the equivalent data point. The modelled values show reasonable agreement with the magnetometer profiles. The modelled data resolved in the radar beam pointing directions, also shows reasonable agreement with the observer latitude profiles and good agreement with the phase of the radar longitude profiles, indicating that the latitudinal and longitudinal scaling of the model is valid.

The spatial variation of the modelled wave field may also be seen in Figs. 1 and 2, where the left-hand columns show theoretical latitude–velocity radar plots for compar-

ison with data. Theoretical velocity values were derived from the cross product of the model perturbation electric field and the background field used in the model (e.g. $\mathbf{v} = \mathbf{E} \times \mathbf{B}_0$). The model values are only plotted at points where data is available and points where data has been identified as ground scatter are marked in grey in both columns of plots. Contour plots showing the spatial variation of the model parameters are presented in Fig. 12, with panels (a)–(e) representing the magnetic field components b_x and b_y , the electric field components E_x , E_y and the FAC j_z , respectively, where the vertical axis represents the north–south (X) direction and the horizontal axis the east–west (Y) direction where negative values are represented by dashed lines and positive values by solid lines. The structure of the FAC in the lower panel clearly shows that near the resonance the current sheets are approximately aligned along lines of constant latitude supporting the assumptions made, when calculating the FAST FAC from the magnetic field data (discussed in Section 4.2).

The model was also used to calculate the magnetic field components and the FAC for the FAST trajectory through the wave field, where both the spatial and temporal variations of the wave field need to be considered. The model values were calculated at the 0.5 s time resolution, taking into account the location and time associated with each data point, producing time series suitable for direct comparison with FAST data. The model magnetic field components are plotted in red alongside observed data in panels (a) and (b) of Fig. 6, and the model FAC has been plotted with the FAC density derived from the particle measurements in panel (g) of Fig. 6. Due to the spatial and temporal variations of both the satellite position and the wave, the model predicts that FAST will actually observe little of the oscillatory variation of the wave. However, the large-scale features observed in the FAST magnetic field measurements are reproduced reasonably well by the model. Note also that many small-scale features which are observed in the FAST data are not included in the model, which is restricted to the large-scale features of the FLR.

5. Discussion

The model applied here is only valid in regions where there is a FLR and therefore closed field lines. In order to identify the regions where the model provides a valid estimate of the fields and currents observed by FAST, the open-closed field line boundary and the equatorward edge of the auroral oval must be identified. Fig. 13 presents a polar-plot of an hourly averaged global convection map of plasma convection for 1100–1200 UT, which was produced by combining the l-o-s velocities from all eight of the Northern hemisphere SuperDARN radars using the map potential technique (Ruohoniemi and Baker, 1998), averaging out the wave field oscillations. Although the flows marked on the convection map are not particularly intense,

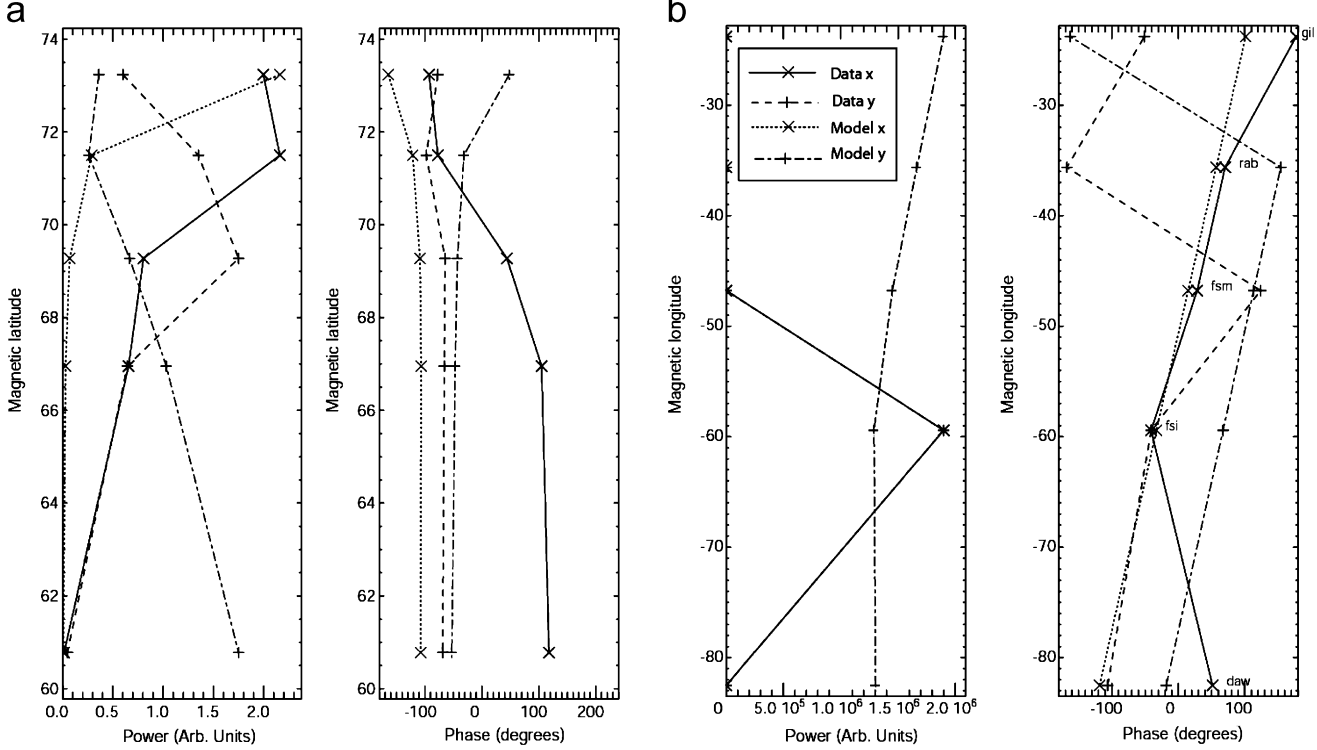


Fig. 10. Latitude and longitude profile power and phase plots for the CANOPUS magnetometer stations. (a) The latitude profile is centred on $\sim -29^\circ$ MLON. (b) The longitude profile, centred on $\sim 67^\circ$ MLAT. The + signs represent the Y components and x signs representing the X components. The solid and dashed lines represent the data x and y components respectively. The dotted and dot-dashed lines represent the model x and y components respectively. For each of the profiles here the information was taken for the frequency 2.2 mHz from Fourier analysis of data for the time interval 11:00–12:30 UT.

they do show a two cell convection pattern, with open field lines moving antisunward across the polar cap and closed field lines returning sunward around the flanks. The boundary between these flows therefore provide an indication that the open-closed field line boundary at ~ 0500 MLT lies between 75 and 78° MLAT.

Fig. 14 shows polar plots of the footprints of DMSP satellite F13 for two crossings of the auroral zones, between 1000–1020 UT and 1140–1200 UT. The particle spectrograms for each crossing were examined. As the spacecraft passes from closed to open field lines it is expected that a sudden drop in the energy of the precipitating particles will be observed (Newell and Meng, 1988, 1995). On open field lines the spacecraft should observe precipitating cusp particles, which are typically of lower energy than those observed on the closed field lines, in the auroral zone. Such drops (from 100 s keV to 100 s eV) were observed in DMSP data and have been used to identify the open-closed field line boundary (OCFLB). The portions of the satellite footprint identified as crossing open field lines, are indicated in Fig. 14 by the solid line. Regions of closed field lines are indicated by dashed lines. During the first crossing, at the dayside, the OCFLB appears to lie at $\sim 77^\circ$ MLAT. During the second crossing, F13 observes a dip in auroral precipitation as it enters the polar cap indicating that the open closed field line boundary is at $\sim 80^\circ$ MLAT. The location of the OCFLB

may also be inferred from a similar drop in the energy of precipitating particles observed in FAST data. Such a drop occurs in the electron energy spectra, shown in panels (c) and (d) of Fig. 6, at ~ 1132 UT and $\sim 77^\circ$ MLAT.

The ionospheric irregularities required for radar backscatter occur predominantly in the auroral zone and have been shown in some situations to provide a reliable indication of its latitudinal location, particularly on the dayside (Milan et al., 1998). The radar l-o-s velocity data presented in Figs. 1 and 2 show good backscatter between $\sim 68^\circ$ and $\sim 75^\circ$ MLAT. The radar backscatter, DMSP data and map potential plot, all suggest that the open closed field line boundary lies at or above 75° MLAT. It is not expected that the FLR will be observed in FAST data at latitudes above the open-closed field line boundary. The analysis presented here concentrates on FAST data after 11:32:15 UT when FAST is known to be crossing closed field lines.

Fig. 15 shows the FAST FAC densities and corresponding modelled values from within this interval. The modelled data, magnetic fields and energetic particle spectra from FAST were all used to calculate the FAC associated with the wave with both the model and field-derived FAC calculated using Eq. (12). In order to improve this calculation, a running mean with a window of 5 s has been used to smooth the data, removing spin effects (spin period ~ 5 s). The resulting currents are presented in Fig. 15. The

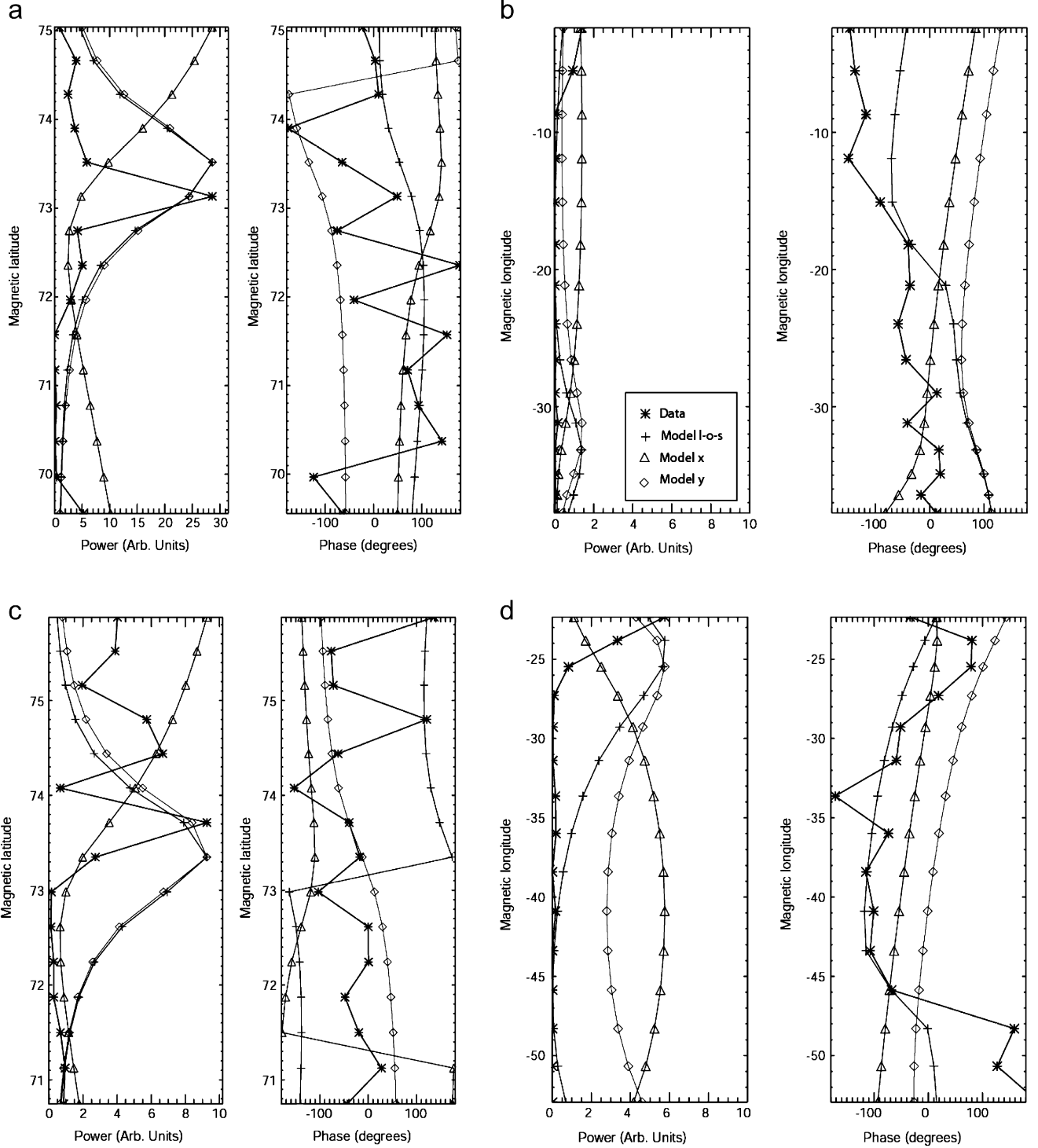


Fig. 11. Latitude and longitude profile power and phase plots for the Kapuskasing and Saskatoon radars. (a) The latitude profile for the Kapuskasing radar, uses data from beam 11, which is centred on $\sim -15^\circ$ MLON. (b) The longitude profile for the Kapuskasing radar, uses data from range gate 35, all beams, centred on $\sim 73^\circ$ MLAT. (c) The latitude profile for the Saskatoon radar uses data from beam 5, which is centred on $\sim -28^\circ$ MLON. (d) The longitude profile for the Saskatoon radar, uses data from range gate 30, all beams centred on $\sim 70^\circ$ MLAT. The star symbols represent the line of sight velocity, the diamonds and triangles represent the model x and y components, respectively, and the crosses represent the model velocity resolved in the direction of the radar line of sight velocity. For each of the profiles here the information was taken for the frequency 2.2 mHz from Fourier analysis of data for the time interval 11:00–12:30 UT.

dotted lines show the currents when smoothed using a running mean window of 30 s. Negative values represent upward FAC.

The modelled current may be divided into two intervals within the region of interest (denoted in Fig. 15 by the grey shading). These two intervals represent

the main peaks of modelled upward and downward FAC, defined by the zero crossing of the modelled FAC at the centre of the interval (near the FLR) and the half

maximum points of the FAC regions on either side of the FAC pair. Interval i is a region of upward current (downgoing electrons), with a peak of $-1.5 \mu\text{A m}^{-2}$ for the model FAC and $-1.3 \mu\text{A m}^{-2}$ for the field-derived FAC. Interval ii is a region of downward FAC with a peak of $+1.5$ and $+1.0 \mu\text{A m}^{-2}$ for the model- and field-derived currents, respectively. There is reasonable agreement between the peak values of modelled and field-derived currents, although clearly small-scale features exist in the field-derived current which are not present in the model. Closer inspection of the field-derived current suggests that the wave field at FAST may not have as large a latitudinal

Table 1
The model scaling parameters

Latitude	73.5°
Period (frequency)	450s (2.2 mHz)
M	3.7
Longitudinal wavelength	3000 km
FWHM	160 km

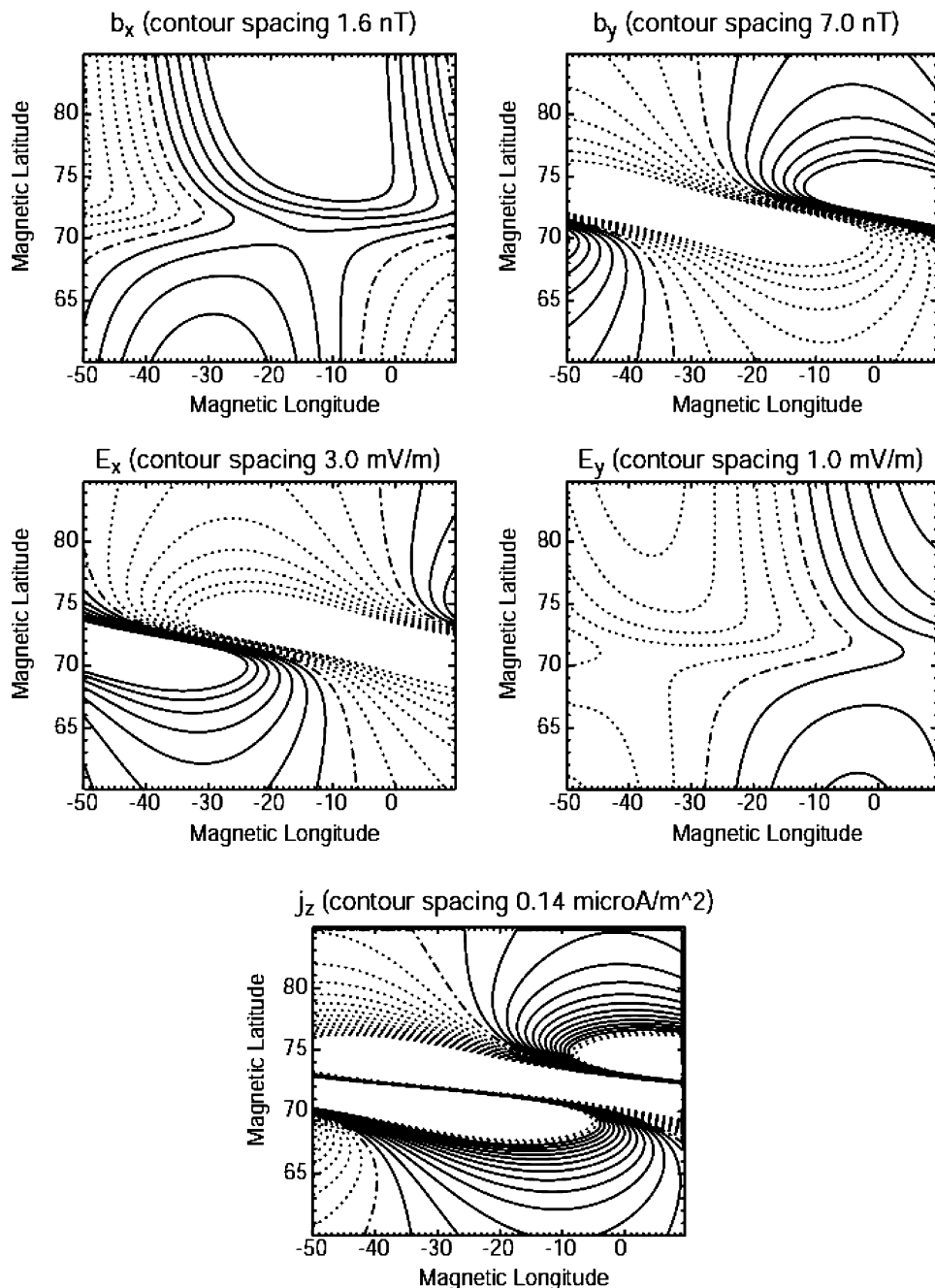


Fig. 12. Contour plots of the magnetic and electric field x and y components (\mathbf{b}_x , \mathbf{b}_y , \mathbf{E}_x , \mathbf{E}_y) and the field-aligned current (j_z) plotted in latitude and longitude, where the position of the resonance is at 70° magnetic latitude.

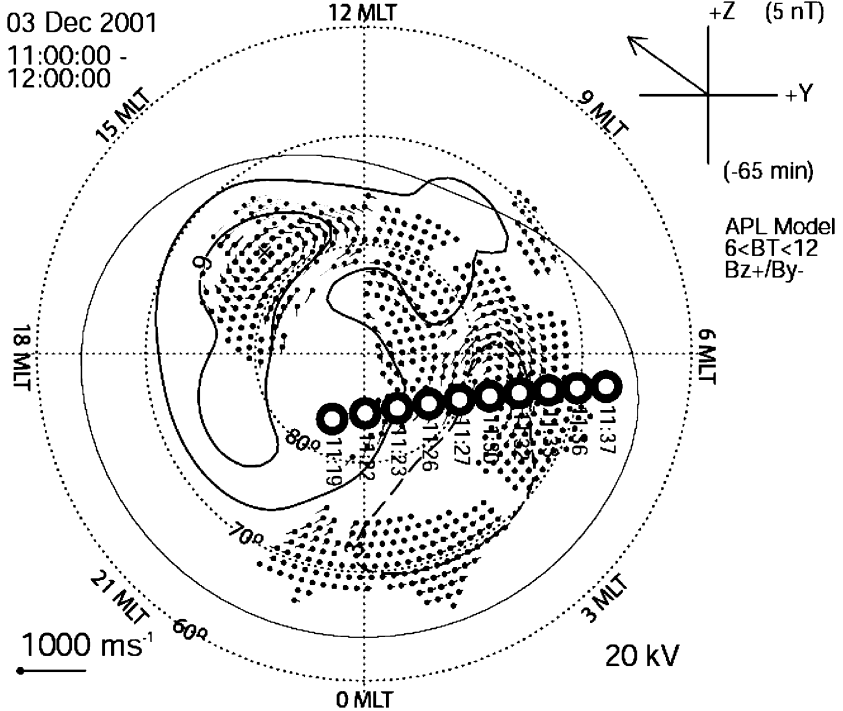


Fig. 13. A polar-plot of an hourly averaged global convection map of plasma convection for 1100–1200 UT, which was produced by combining the line of site (l-o-s) velocities the Northern hemisphere SuperDARN radars using the map potential technique. The thick black line marks the location of the Heppner–Maynard boundary. The velocity vectors are marked by the shorter lines, where length indicates the magnitude of the velocity.

scale length as was suggested by the ground-based observations.

Integrating along the spacecraft path within each of these regions provides a better indication of the agreement between the measured and modelled currents. The integrated values of the FAC are presented in Table 2. In interval I, the model- and field-derived current integration values are -119 and $-23 \mu\text{A m}^{-1}$, respectively. For interval ii, the model and field-derived current integration values are $+117$ and $+25 \mu\text{A m}^{-1}$. These comparisons indicate that the observed large-scale currents agree in sign with those predicted by the MHD model for the major current intervals, but the model currents are significantly larger than those predicted by the data. However, many small dipolar regions with a scale size of between 13 and 52 km, which are not predicted by MHD, exist within the large-scale current. The scale size of these features was obtained using an automated process which flagged each peak in the data, which had been smoothed using a 5 s running mean window. As a result small-scale features with scale sizes covered by the spacecraft in less than one spin period (~ 5 s) will not be recognised.

It should be noted that the upward current portions of the field- and particle-derived currents, which are carried primarily by hot downgoing magnetospheric electrons, agree relatively well. The particle-derived current fails to show the majority of the downward FAC present in the field-derived FAC, which is carried by cold upwelling ionospheric electrons, the majority of which have energies

below the energy detection threshold of the FAST particle instruments (5 eV). It should therefore be noted that although values for the integration of the particle-derived current have been included in Table 2, it is unrealistic to make direct comparisons with the integrations of the model- and particle-derived currents. Since very little downward FAC is measured, the values are biased towards upward FAC.

Fig. 16 shows the current contributions from electrons of different energies calculated directly from the particle spectra, with panels (a)–(e) representing the contributions from electrons in the energy bands 5–30 eV, 30–500 eV, 500 eV–1 keV, 1–3.5 keV, and 3.5–40 keV, respectively, and panel (f) representing the total FAC. Some evidence of downward FAC (upgoing electrons) is observed in the 5–30 eV energy band particularly at ~ 1133 UT. The $1.5 \mu\text{A m}^{-2}$ upward current peak in the model-and field-derived currents, located between 1132 and 1134 UT appears to have a contribution to the current carried by electrons in the range 500 eV–3.5 keV, with a small contribution from electrons in the highest energy band 3.5–40 keV. One might expect to see the downward acceleration of higher energy electrons during interval i, in order to carry the upward FAC observed in the model- and field-derived current, followed by a decrease in the downward acceleration of electrons and observations of colder, upwards accelerated electrons during interval ii, which shows a downward FAC peak ($\sim 1.5 \mu\text{A m}^{-2}$) in the model-derived currents. However electrons in the 500 eV

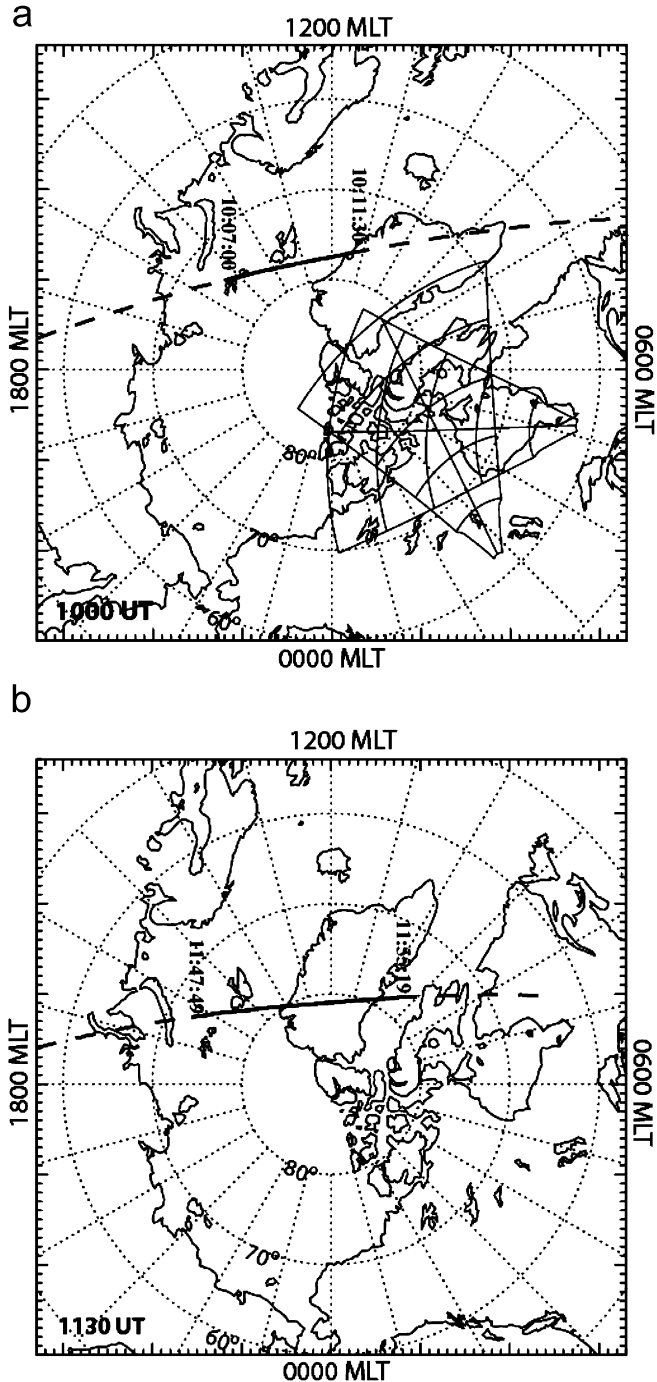


Fig. 14. Polar plots, showing the footprint of the DMSP satellite F13 during two polar crossings. The dashed black lines indicate the portions of the orbit where very little energetic particle precipitation occurs. The solid black lines indicate regions of intense energetic particle precipitation: (a) 1000 UT and (b) 1130 UT.

–3.5 keV energy band continue to supply upward FAC during interval ii, with their largest current spikes in this interval. It is possible that this feature is related to the small-scale oscillations in the data, which appear at the start of the interval. The current contribution from the ions is insignificant and is therefore not presented here.

6. Comparison with dusk sector wave

How does this dawn sector wave (~ 0500 MLT) (wave 2) compare with the dusk sector wave (~ 1900 MLT) (wave 1) discussed in Scofford et al. (2005)? The wave fields are imposed upon opposite sense region 1–region 2 current systems. Wave 2 has a smaller period of 450 s, compared to 750 s for wave 1. Wave 2 also has a smaller azimuthal variation, with an $m \sim 4$, compared to $m \sim 7$ for the dusk sector wave, which correspond 360° of phase change over 1900 and 3000 km, respectively. Wave 1 is centred on 71° MLAT and Wave 2 is centred on 74° MLAT. Wave 1 is spread over 10° of latitude with a larger latitudinal scaling and a FWHM of 350 km. Wave 2 is spread over 5° of latitude with a FWHM of ~ 160 km. In wave 1 more than 180° of phase change was observed over the resonance suggesting that the wave was in a transitional state. Wave 2 is generally a more classical FLR, showing only 180° of phase change over the resonance as one might expect of a FLR in a steady state.

In both cases, an MHD model, based on the ground data (radar and magnetometer) makes a reasonably reliable prediction of the large-scale wave features observed in the FAST data, with many small-scale features also present in the data which are not included in the model. The integrated field-derived FACs agree, at least in sign, with the integrated model values, although the magnitude of the model currents exceeds that of the field-derived current data. For wave 2, the discrepancy was a factor of 5, while in wave 1 a factor of 2 was observed. The data also indicates the presence of small bipolar regions of current which exist within the large-scale structure which may be related to inertial affects, which become significant at altitudes corresponding to the peak in Alfvén speed (see Scofford et al., 2005, Fig. 10). The scale size of these features corresponds to approximately ten electron inertial lengths ($\lambda_e = \sqrt{m_e/\mu_0 n_e e^2}$) and is consistent with observations of similar features made in other studies (Stasiewicz et al., 1997; Drozdenko and Morales, 2000). Features with scale sizes of one inertial length and smaller are also commonly observed (e.g. Stasiewicz et al., 2000). Ten electron inertial lengths is also the lower limit that can be achieved through phasemixing before radiation as inertial Alfvén waves prevents further phasemixing (Wei et al., 1994; Damiano et al., 2003).

The particle acceleration which leads to the small-scale FAC features is likely to affect the ionospheric conductivity, possibly causing sharp gradients (Lysak and Song, 2002; Streltsov and Lotko, 2004). In turn, the conductivity will affect the flow of FAC associated with the wave field. The conductivity has been assumed to be constant for the purposes of the model and this will introduce inaccuracies into the model output.

The model currents used for both waves was based purely on the modelled wave parameters, and contained no information about background upward and downward FACs due to the region 1 and region 2 current systems

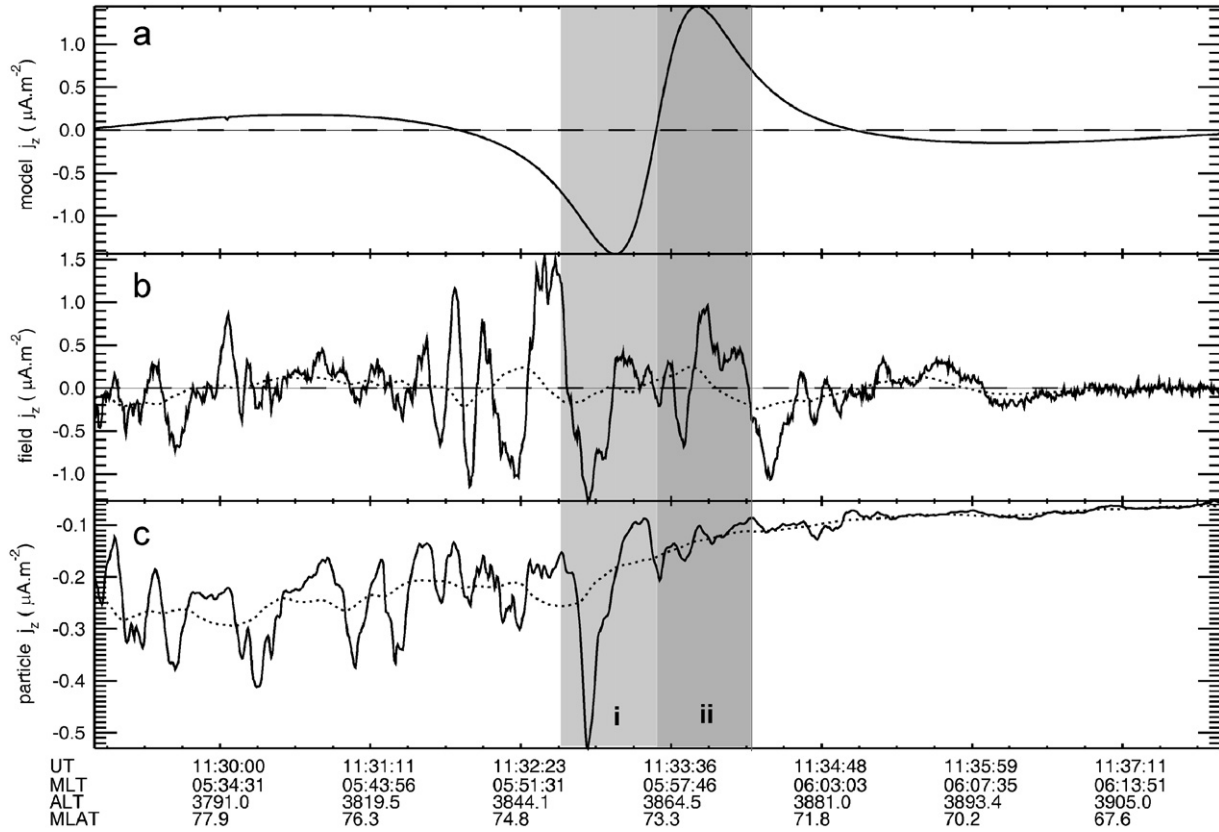


Fig. 15. The field-aligned current calculated from the model and from FAST field and particle data. Negative values represent upward field-aligned current. The field- and particle-derived currents have been smoothed using a 5 s running mean. The dotted lines show the same currents smoothed with a 30 s running mean. The grey lines indicate the zero axes. The shading indicates the division of the time interval into two smaller intervals, as labelled.

Table 2
The integrated values

Interval	Model $\int j_z \, ds$ (mA m ⁻¹)	Field $\int j_z \, ds$ (mA m ⁻¹)	Particle $\int j_z \, ds$ (mA m ⁻¹)
i (11:33:43–11:33:29 UT)	-119	-23	-23
ii (11:33:29–11:34:14 UT)	117	25	-15

(Iijima and Potemra, 1976). Clearly such current systems will be present in the data and typical magnetic field perturbations of 100 nT result in FAST data (Carlson et al., 1998b). For both waves, the pattern of FAC observed is clearly more structured than a typical region 1–region 2 current system and is consistent with the traversal of a FLR. The FAC structures associated with the wave 1 and wave 2 FLRs, would have been imposed on opposite sense region 1–region 2 current systems. However, in both cases the model values provide a reasonable estimate of the FAST measured FACs.

For both waves, the majority of the upward moving electrons which carry the downward current are not observed by the FAST particle instruments though their presence is indicated by the field-derived currents. There is a small downward FAC measured in the lowest electron energy band <30 eV; however, it is expected that

most of the electrons which carry the downward FAC are below the 5 eV energy detection threshold of the FAST particle instruments. Thus, neither case provides any evidence for the upward acceleration of electrons in the regions carrying current densities of up to 1.5 $\mu\text{A m}^{-2}$, indicating that the electron density in this region is high enough to carry the downward current without any significant acceleration of electrons at and below the altitude of FAST.

In both waves, downward moving magnetospheric electrons with energies between 5 and 500 eV are observed to carry the upward FAC. In wave 1, there were no large peaks inferred in the upward FAC expected over the FAST footprint. Wave 2 has a much smaller latitudinal scale and FAST flies through the wave field at a time when the phasing results in the observation of higher upward current densities. During a peak in upward FAC of $\sim 1.5 \mu\text{A m}^{-2}$,

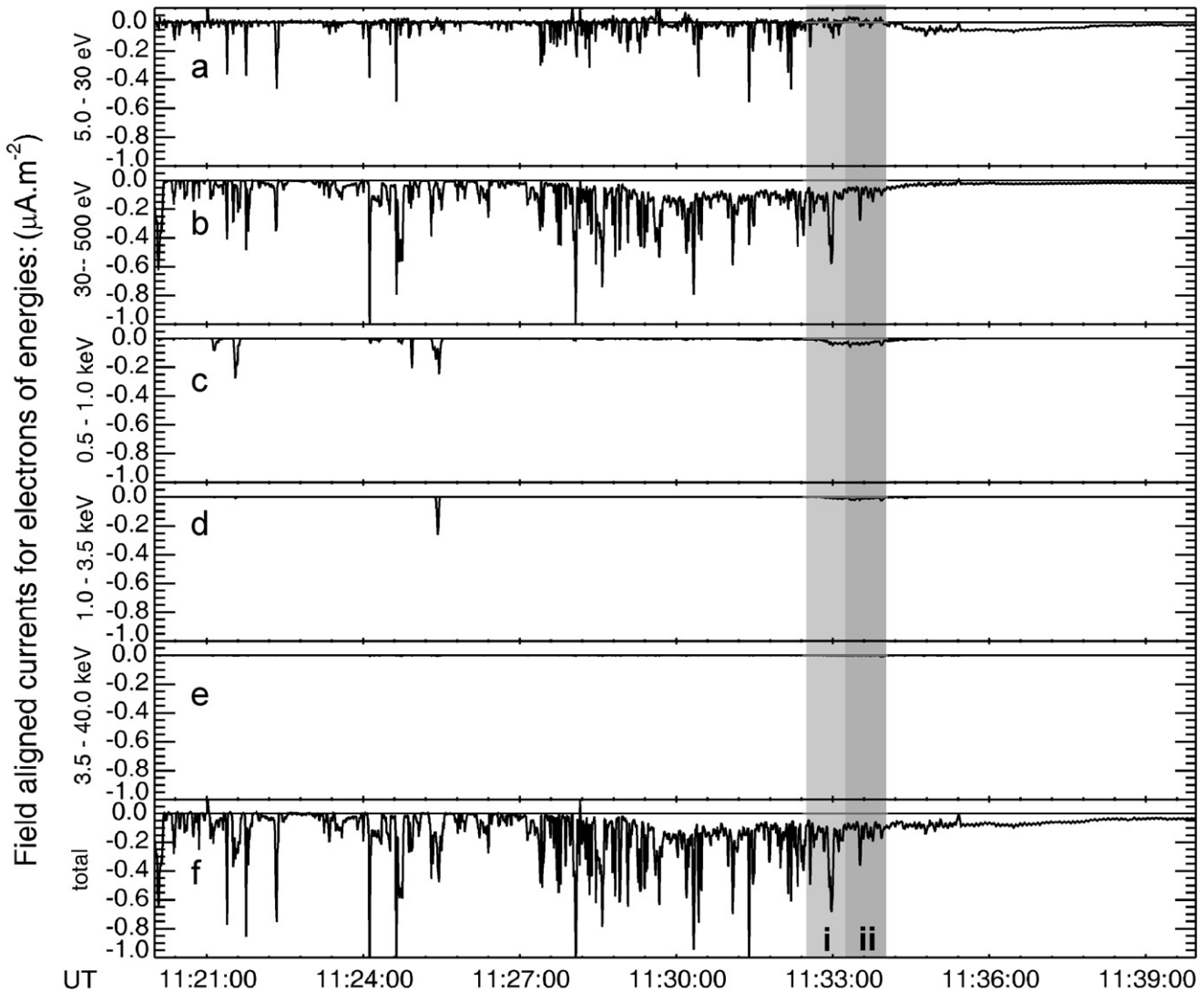


Fig. 16. Current contributions from electrons of different energies. Panel (a) represents the current contribution from electrons with energies between 5 and 30 eV. Panels (b), (c), (d) and (e) represent the current contributions from electrons in the energy ranges 30–500 eV, 500 eV–1 keV, 1–3.5 keV and 3.5–40.0 keV, respectively. Panel (f) represents the sum of these currents. Negative values indicate upward field-aligned current. Current intervals i and ii are denoted by the grey shading.

in interval i, FAST observes some downward accelerated electrons in the 500 eV–3.5 keV energy range. It is thought that maximum energisation of electrons occurs at the altitude of the B/n peak (the peak in Alfvén speed), which is found to be $\sim 1R_E$ (~ 3000 km above FAST) and that the acceleration of the electrons which carry the upward FAC associated with FLRs occurs in an accelerator region which extends around $1R_E$ above this peak (Streltsov and Lotko, 1997). Similar properties are reported by Vedin and Rönnmark (2004). Chaston et al. (2003) showed that most electron acceleration occurs at altitudes between 1 and $2R_E$ with the most energetic electrons arriving from altitudes between 2 and $3R_E$ and hence more electron acceleration occurs above the FAST than below it. It is therefore expected that the electrons observed by FAST (at ~ 3000 km altitude) have already undergone acceleration in this region.

7. Summary

The longitudinal and latitudinal phase and amplitude profiles of a large-scale ULF wave event have been determined from observations made by the Kapuskasing and Saskatoon radars of the SuperDARN chain and the CANOPUS and Greenland magnetometer arrays, and have been used to scale a simple model of an Alfvénic FLR, which predicts the FAC distributions expected from a purely MHD Alfvén wave. The FAST satellite passed through the radar field of view as the wave occurred, measuring the magnetic field oscillations of the wave at around 3500 km altitude, along with the precipitating ion and electron populations associated with these fields. This conjunction offered the opportunity to examine the large-scale and small-scale FAC systems associated with the large-scale Alfvén wave in the dawn sector, determine the

particles responsible for carrying these FACs and compare it with the dusk sector wave discussed in Scoffield et al. (2005).

As with the dusk sector wave study, the model displays reasonable large-scale agreement with FAST observations. The modelled and observed FAC have been compared and the particle measurements have been studied. The interval studied was divided into two smaller intervals, labelled i and ii, depending on the net flow of FAC, with the intervals showing: an upward current peak ($\sim 1.5 \mu\text{A m}^{-2}$) and a downward current peak ($\sim 1.5 \mu\text{A m}^{-2}$), respectively.

The majority of upward FAC appears to be carried by electrons with energies $< 500 \text{ eV}$; however, some downward acceleration of electrons of higher energies between 500 eV and 3.5 keV is observed during the $1.5 \mu\text{A m}^{-2}$ upward current peak of interval i. No upward acceleration of electrons with energies in excess of 30 eV is observed despite the downward current peaks observed in the field-derived currents, supporting evidence from the dusk wave study that suggested that the majority of downward current carriers were of energies below FAST's detection threshold of 5 eV . Again small-scale structuring is imposed on the current carriers, possibly resulting from inertial effects, which become important at FAST altitudes (when the wave is best thought of as an inertial Alfvén wave rather than an idealised MHD Alfvén wave). It is clear that small-scale physics is operating but is not observed by ground magnetometers and radar instruments. Further work is required to characterise the nature and scale size of these features.

In general, the findings of this dawn sector wave study support those of the dusk sector wave study (Scoffield et al., 2005). The study of multiple additional FLRs is required to define how typical such behaviour is and how current carrying particles in large-scale magnetospheric FLRs are affected by latitudinal and longitudinal scaling and background current systems. Despite the wealth of FAST and SuperDARN data available, to-date it has not been possible to identify any events with ground and spacecraft data of sufficient quality for such a study to be carried out. Two further events have been identified as suitable for such analysis. The first (Wave 3) has a FAC structure similar to that of Wave 1 and was located in the dawn sector. The second (Wave 4), also located in the dawn sector had a FAC structure similar to Wave 2, with a very large longitudinal scaling ($m \sim 1$). The analysis of Waves 3 and 4 showed good agreement with Waves 1 and 2, with the modelled and field-derived current intervals, defined as in Section 5, agreeing in sign, but with the integrated model values exceeding the integrated field-derived current by a factor of 2 or 3 for these wave events, supporting the findings discussed above.

Acknowledgments

H.C. Scoffield is supported by a research studentship from the UK's Particle Physics and Astronomy Research

Council (PPARC). D.M. Wright is supported by a PPARC advanced fellowship. R.J. Strangeway is supported by NASA Grant NAG5-12590 and NSF grant ATM-0208498. CUTLASS is a PPARC UK National Facility operated by the University of Leicester under Grant PPA/R/R/1997/00256.

The Saskatoon radar, Canada, is operated by the University of Saskatchewan and the Kapuskasing radar is operated by the Johns Hopkins Applied Physics Laboratory, USA. The DMSP particle detectors were designed by Dave Hardy of AFRL, and data obtained from JHU/APL. We thank Dave Hardy, Fred Rich, and Patrick Newell for its use.

The CANOPUS instrument array constructed, maintained and operated by the Canadian Space Agency, provided some of the magnetometer data used in this study.

Many thanks to Dr. Jurgen Watermann, of the Danish Meteorological Institute (DMI) for providing Greenland magnetometer data and to Dr. A. Grocott, University of Leicester for his help in producing Fig. 13.

References

- Anderson, B.J., Engebretson, M.J., Rounds, S.P., Zanetti, L.J., Potemra, T.A., 1990. A statistical study of Pc 3–5 pulsations observed by the AMPTE/CCE magnetic fields experiment 1. Occurrence distribution. *J. Geophys. Res.* 95, 10,495–10,523.
- Baddeley, L.J., Yeoman, T.K., Wright, D.M., Davies, J.A., Trattner, K.J., Roeder, J.L., 2002. Morning sector drift–bounce resonance driven ULF waves observed in artificially-induced HF radar backscatter. *Ann. Geophys.* 20, 1,487–1,498.
- Carlson, C.W., Pfaff, R.F., Watzin, J.G., 1998a. The Fast Auroral Snapshot (FAST) mission. *Geophys. Res. Lett.* 25, 2,013–2,016.
- Carlson, C.W., McFadden, J.P., Ergun, R.E., Temerin, M., Peria, W., Mozer, F.S., Klumpar, D.M., Shelley, E.G., Peterson, W.K., Moebius, E., Elphic, R., Strangeway, R., Cattell, C., Pfaff, R., 1998b. FAST observations in the downward auroral current region: Energetic upgoing electron beams, parallel potential drops and ion heating. *Geophys. Res. Lett.* 25, 2,017–2,020.
- Carlson, C.W., McFadden, J.P., Turin, P., Curtis, D.W., 2001. The Electron and Ion Plasma Experiment for FAST. *Space Sci. Rev.* 98, 33–66.
- Chaston, C.C., Bonnell, J.W., Carlson, C.W., McFadden, J.P., Ergun, R.E., Strangeway, R.J., 2003. Properties of small-scale Alfvén waves and accelerated electrons from FAST. *J. Geophys. Res.* 108, 8003.
- Chen, L., Hasegawa, A., 1974a. A theory of long-period magnetic pulsations 1. Steady state excitation of field line resonances. *J. Geophys. Res.* 79, 1,024–1,032.
- Chen, L., Hasegawa, A., 1974b. A theory of long-period magnetic pulsations 2. Impulse excitation of surface eigenmode. *J. Geophys. Res.* 79, 1,032–1,037.
- Damiano, P.A., Sydora, R.D., Samson, J.C., 2003. Hybrid magnetohydrodynamic-kinetic model of standing shear Alfvén waves. *J. Plasma Phys.* 69, 277–304.
- Drozdenco, T., Morales, G.J., 2000. Interaction of a shear Alfvén wave with a filamentary density perturbation in a low β -plasma. *Phys. Plasmas* 7, 823–830.
- Elphic, R.C., Bonnell, J.W., Strangeway, R.J., Kepko, L., Ergun, R.E., McFadden, J.P., Carlson, C.W., Peria, W., Cattell, C.A., Klumpar, D., Shelley, E., Peterson, W., Moebius, E., Kistler, L., Pfaff, R., 1998. The auroral current circuit and field-aligned currents observed by FAST. *Geophys. Res. Lett.* 25, 2,033–2,036.

- Ergun, R.E., Cerson, C.W., Mozer, F.S., Delory, G.T., Temerin, M., McFadden, J.P., Pankow, D., Abiad, R., Harvey, P., Wilkes, R., Primsch, H., 2001. The FAST satellite fields. *Space Sci. Rev.* 98, 67–91.
- Fenrich, F.R., Samson, J.C., 1997. Growth and decay of field line resonances. *J. Geophys. Res.* 102, 20,031–20,039.
- Fenrich, F.R., Samson, J.C., Sofko, G., Greenwald, R.A., 1995. ULF high- and low- m field line resonances observed with the Super Dual Auroral Radar Network. *J. Geophys. Res.* 100, 21,535–21,547.
- Greenwald, R.A., Baker, K.B., Dudeney, J.R., Pinnock, M., Jones, T.B., Thomas, E.C., Villain, J.-P., Cerrier, J.-C., Senior, C., Hanuise, C., Hunsucker, R.D., Sofko, G., Koehler, J., Nielsen, E., Pellinen, R., Walker, A.D.M., Sato, N., Yamagishi, H., 1995. DARN/SUPER-DARN a global view of the dynamics of high-latitude convection. *Space Sci. Rev.* 71, 761–796.
- Iijima, T., Potemra, T.A., 1976. The amplitude distribution of field-aligned currents at northern high latitudes observed by TRIAD. *J. Geophys. Res.* 81, 2,165–2,174.
- Liu, W.W., Xu, B.-L., Samson, J.C., Rostoker, G., 1995. Theory and observation of auroral substorms: a magnetohydrodynamic approach. *J. Geophys. Res.* 100 (A1), 79–95.
- Lotko, W., Streltsov, A.V., Carlson, C.W., 1998. Discrete auroral arc, electrostatic shock and superthermal electrons powered by dispersive, anomalously resistive field line resonance. *Geophys. Res. Lett.* 25 (24), 4,449–4,452.
- Lysak, R.L., Song, Y., 2002. Energies of the ionospheric feedback interaction. *J. Geophys. Res.* 107, 1160–1171.
- Milan, S.E., Yeoman, T.K., Lester, M., 1998. The dayside auroral zone as a hard target for coherent HF radars. *Geophys. Res. Lett.* 25, 3717–3720.
- Milan, S.E., Sato, N., Ejiri, M., Moen, J., 2001. Auroral forms and the field-aligned current structure associated with field line resonances. *J. Geophys. Res.* 106, 25,825–25,833.
- Newell, D.A., Meng, C.-I., 1988. The cusp and the cleft/boundary layer: low-altitude identifications and statistical local time variation. *J. Geophys. Res.* 93, 14,549.
- Newell, D.A., Meng, C.-I., 1995. Cusp low-energy ion cutoffs: a survey and implications for merging. *J. Geophys. Res.* 100, 21,943.
- Peria, W.J., Carlson, C.W., Ergun, R.E., McFadden, J.P., 2000. Characteristics of field-aligned currents near the auroral acceleration region: FAST observations. *AGU Geophys. Monogr.* 118, 181–189.
- Rankin, R., Tikhonchuk, V.T., 1998. Numerical simulations and simplified models of nonlinear electron inertial Alfvén waves. *J. Geophys. Res.* 103, 20,419–20,433.
- Rankin, R., Samson, J.C., Tikhonchuk, V.T., Voronkov, I., 1999a. Auroral density fluctuations in dispersive field line resonances. *J. Geophys. Res.* 104, 4399–4410.
- Rankin, R., Samson, J.C., Tikhonchuk, V.T., 1999b. Discrete auroral arcs and nonlinear dispersive field line resonances. *Geophys. Res. Lett.* 26, 663–666.
- Rankin, R., Fenrich, F., Tikhonchuk, V.T., 2000. Shear Alfvén waves on stretched magnetic field lines near midnight in Earth's magnetosphere. *Geophys. Res. Lett.* 27, 3265–3268.
- Ruohoniemi, J.M., Baker, K.B., 1998. Large-scale imaging of high-latitude convection with Super Dual Auroral Radar Network HF radar observations. *J. Geophys. Res.* 103, 20,797–20,811.
- Ruohoniemi, J.M., Greenwald, R.A., Baker, K.B., 1991. HF radar observations of Pc5 field line resonances in the midnight/early morning MLT sector. *J. Geophys. Res.* 96, 15,697–15,710.
- Samson, J.C., Rostoker, G., 1972. Latitude-dependent characteristics of high-latitude Pc 4 and Pc 5 micropulsations. *J. Geophys. Res.* 77, 6,133–6,144.
- Samson, J.C., Hughes, T.J., Creutzberg, F., Wallis, D.D., Greenwald, R.A., Ruohoniemi, J.M., 1991. Observations of a detached, discrete arc in association with field line resonances. *J. Geophys. Res.* 96 (A9), 15,683–15,695.
- Samson, J.C., Wallis, D.D., Hughes, T.J., Creutzberg, F., Ruohoniemi, J.M., Greenwald, R.A., 1992. Substorm intensifications and field line resonances in the nightside magnetopause. *J. Geophys. Res.* 97 (A6), 8,495–8,518.
- Samson, J.C., Cogger, L.L., Pao, Q., 1996. Observations of field line resonances, auroral arcs and auroral vortex structures. *J. Geophys. Res.* 101 (A8), 17,373–17,383.
- Scofield, H.C., Yeoman, T.K., Wright, D.M., Milan, S.E., Wright, A.N., Strangeway, R.J., 2005. An investigation of the field aligned currents associated with a large scale ULF wave using data from CUTLASS and FAST. *Ann. Geophys.* 23, 487–498.
- Southwood, D.J., 1974. Some features of field line resonances in the magnetosphere. *Planet. Space Sci.* 22, 483–491.
- Stasiewicz, K., Gustafsson, G., Marklund, G., Lindqvist, P.-A., Clemmons, J., Zanetti, L., 1997. Cavity resonators and Alfvén resonance cones observed on Freja. *J. Geophys. Res.* 102 (2), 565–2575.
- Stasiewicz, K., Khotyaintsev, Y., Berthomier, M., Wahlund, J.-E., 2000. Identification of widespread turbulence of dispersive Alfvén waves. *Geophys. Res. Lett.* 27, 173–176.
- Streltsov, A.V., Lotko, W., 1995. Dispersive field line resonances on auroral field lines. *J. Geophys. Res.* 100, 19,457–19,472.
- Streltsov, A.V., Lotko, W., 1996. The fine structure of dispersive, nonradiative field line resonance layers. *J. Geophys. Res.* 101, 5343–5358.
- Streltsov, A.V., Lotko, W., 1997. Dispersive, nonradiative field line resonances in a dipolar magnetic field geometry. *J. Geophys. Res.* 101, 27,121–27,136.
- Streltsov, A.V., Lotko, W., 1999. Small-scale, “electrostatic” auroral structures and Alfvén waves. *J. Geophys. Res.* 104 (A3), 4411–4426.
- Streltsov, A.V., Lotko, W., 2004. Multiscale electrodynamics of the ionosphere–magnetosphere system. *J. Geophys. Res.* 109 (A09214).
- Streltsov, A.V., Lotko, W., Johnson, J.R., Cheng, C.Z., 1998. Small-scale, dispersive field line resonances in the hot magnetospheric plasma. *J. Geophys. Res.* 103, 26,559–26,572.
- Sugiura, M., Wilson, C.R., 1964. Oscillations of the geomagnetic field lines and associated magnetic perturbations at conjugate points. *J. Geophys. Res.* 69, 1211–1216.
- Vedin, J., Rönnmark, K., 2004. A linear auroral current–voltage relation in fluid theory. *Ann. Geophys.* 22, 1719–1728.
- Walker, A.D.M., Greenwald, R.A., Stuart, W.F., Green, C.A., 1979. Stare Auroral Radar observations of Pc5 geomagnetic pulsations. *J. Geophys. Res.* 84, 3,373–3,388.
- Walker, A.D.M., Ruohoniemi, J.M., Baker, K.B., Greenwald, R.A., 1992. Spatial and temporal behaviour of ULF pulsations observed by the Goose Bay HF radar. *J. Geophys. Res.* 97, 12,187–12,202.
- Wei, C.Q., Samson, J.C., Rankin, R., Frycz, P., 1994. Electron inertial effects on geomagnetic field line resonances. *J. Geophys. Res.* 99, 11,265–11,276.
- Wilhjelm, J., Friis-Christensen, 1976. Electric fields and high latitude zonal currents induced by merging of field lines. *Geophys. Pap R-13. Dan. Meteorol. Inst., Charlottenlund, Denmark.*
- Wright, A.N., Allan, W., 1996. Structure, phase motion, and heating within Alfvén resonances. *J. Geophys. Res.* 101, 17,399–17,408.
- Wright, A.N., Hood, A.W., 2003. Field-aligned electron acceleration in Alfvén waves. *J. Geophys. Res.* 108 (A3), 1,135–1,144.
- Wright, D.M., Yeoman, T.K., 1999. High resolution bistatic HF radar observations of ULF waves in artificially generated backscatter. *Geophys. Res. Lett.* 26 (18), 2825–2828.
- Wright, A.N., Allan, W., Ruderman, M.S., Elphic, R.C., 2002. The dynamics of current carriers in standing Alfvén waves: parallel electric fields and the auroral acceleration region. *J. Geophys. Res.* 107 (10), 1,029–1,043.
- Xu, B.-L., Samson, J.C., Lie, W.W., 1993. Observations of optical aurora modulated by resonant Alfvén waves. *J. Geophys. Res.* 98 (A7), 11,531–11,541.
- Yeoman, T.K., Wright, D.M., 2001. ULF waves with drift resonance and drift–bounce resonance energy sources as observed in artificially-induced HF radar backscatter. *Ann. Geophys.* 19, 159–170.